# Chapter 5

# Numerical modeling of ebb-tidal deltas

**Abstract**

Results are presented of experiments performed with a numerical morphodynamic model in order to gain more fundamental knowledge about ebb-tidal deltas. The model simulates waves (SWAN code), tides (Delft3D-flow code), sand transport and sand balance in a coastal sea bounded by a straight coast that is interrupted by one inlet. The model has first been used to confirm conclusions of an earlier study (Chapter 3 of this thesis), which was based on a much more idealized model, that ebb-tidal deltas can be modeled as equilibrium solutions (steady bottom pattern). These deltas resemble observed ebb-tidal deltas, but they do not fold around the deep ebb-dominant channel and their sand volume is a factor 5 smaller than observed sand volumes. Therefore, the dependence of characteristics of modeled ebb-tidal deltas has been investigated on processes that were not accounted for in the idealized model, viz. tidal asymmetry, dissipation of momentum due to a quadratic bottom stress and wave height variations due to shoaling and refraction. It is found that internally generated nonlinear tides hardly affect the characteristics of the deltas. In contrast, prescribing ebb(flood)-dominant tidal currents in the inlet leads to more (less) pronounced delta. Including a quadratic (rather than a linear) bottom stress leads to ebb-tidal deltas of which both the spatial pattern and the sand volume are in reasonable agreement with observed ebb-tidal deltas. This resemblance becomes even more satisfactory if shoaling and refraction of waves are accounted for.

# 5.1   Introduction

Ebb-tidal deltas are morphologic structures situated at the seaward side of tidal inlets. They are observed in many parts of the world (*Ehlers*, 1988; *Davis*, 1997; *Hicks et al.*, 1999; *FitzGerald*, 1996). The ebb-tidal delta is located at the end of the ebb-dominant channel (i.e., stronger peak ebb currents than peak flood currents) and is relatively shallow. It is flanked by two adjacent flood-dominant channels. Analysis of field observations (*Walton and Adams*, 1976; *Hayes*, 1975; *Sha*, 1989a) indicate that the characteristics of ebb-tidal deltas strongly depend on the magnitudes of tidal currents (both the cross-shore and the alongshore component) and on the characteristics of the incoming waves. Because of the large variation in strength of tides and waves, the deltas have been classified in accordance with their external forcing (*Gibeaut and Davis Jr.*, 1993). The aim of this study is to improve our understanding of the physical mechanisms that maintain ebb-tidal deltas. To limit the scope of this study the focus is on tide-dominated ebb-tidal deltas which are characterized by small shore-parallel tidal currents with respect to the cross-shore tidal currents. Such deltas are almost symmetrical with respect to the mid-axis of the inlet and are the simplest features that can be studied. Prototypes of these deltas can be found along the US east coast, see Chapter 1 and 3.

In Chapter 3 an idealized model was developed and used to show that TD and METD ebb-tidal deltas can be modeled as morphodynamic equilibria (i.e., the bottom patterns do not evolve). The model calculates the feedback between a sandy bottom, tidal currents and waves. Instead of performing time integrations to study the time evolution of ebb-tidal deltas, a continuation technique was used to directly calculate morphodynamic equilibria. The modeled channel-shoal patterns compared reasonably well with those of observed symmetric, tide-dominated deltas. In the center of the tidal inlet an ebb-dominant channel is found and at its seaward end the delta is located. This delta is flanked by two flood-dominant channels. In addition, the observed (almost linear) relation between the tidal prism and ebb-tidal sand volume was recovered with the model. However, differences were noticed as well. First, the modeled ebb-dominant channel was less deep and did not protrude as far seaward as observed ones. Second, observations show that the delta is folded around the ebb channel (see Figure 1.2). This was not recovered with the idealized model. Third, the modeled ebb tidal sand volumes were a factor $\sim 5$ smaller than observed volumes. These differences might be caused by the assumptions and limitations in the wave and current model and in the sediment transport model. The currents were modeled by using a rigid lid approximation and a linearized bottom shear-stress formulation. The enhanced bottom friction experienced by currents due to the presence of waves was modeled in a heuristic manner. Furthermore, higher harmonics of the tide were not accounted for. The wave model does not allow for spatial variations in the wave height due to shoaling and refraction of the waves. Furthermore, it was assumed that the waves are in shallow water.

To verify the conclusions obtained with the idealized model, numerical morphodynamic process-based models are needed. They include processes that were not accounted for by the idealized model. Previous studies show that the numerical morphodynamic models have become accurate enough to simulate the evolution of ebb-tidal deltas (*Cayocca*, 2001; *van Leeuwen et al.*, 2003; *Siegle et al.*, 2004). Although the study of *van Leeuwen et al.*

(2003) suggests the evolution of the ebb-tidal delta towards morphodynamic equilibrium, the existence of such equilibria have never been convincingly demonstrated with such numerical morphodynamic models. This might be caused by the fact that they perform time integrations to study the temporal evolution of the bed under influence of waves and currents. The results of the idealized models show that a continuation method is a successful technique to calculate morphodynamic equilibria. The continuation method has never been used within numerical process-based morphodynamic models.

The objectives of this study are therefore twofold. The first one is to verify the conclusions obtained with the idealized model. An equilibrium solution of an ebb-tidal delta is calculated by using a numerical morphodynamic model. The characteristic of the ebb-tidal delta are compared with those of the idealized model and with observations. The second objective is to study the sensitivity of the characteristics of the equilibrium to processes which were not accounted for in the idealized model: tidal asymmetry, dissipation of momentum due to a quadratic bottom shear-stress and effects of waves obtained from a wave model which accounts for refraction and shoaling of waves.

This chapter proceeds along the following lines. In Section 5.2 the mathematical formulations of water motion, sediment transport, sediment mass balance and morphodynamic equilibrium are discussed. In Section 5.3 a description of the solution procedure and the numerical tools is given. The results of the experiments performed are presented in Section 5.4. In Section 5.5 the results are compared with observations and with the results of the idealized model. Section 5.7 contains a discussion and the conclusions.

## 5.2   Model formulation

The morphodynamic model consists of several modules, each accounting for different processes (water motion, sediment transport and bottom changes). A sketch of the model structure is given in Figure 5.1. Starting point is a domain with an erodible bottom. Next, the waves and currents are calculated. The currents and waves transport the sediment. Spatial differences in this sediment transport give rise to bottom changes. Since the currents and waves are altered by this new bottom, the loop starts again. In this section the various modules of the morphodynamic model are discussed.
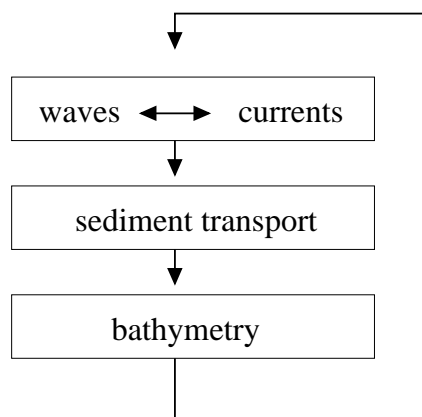


Figure 5.1:   Schematic representation of the numerical morphodynamic model.

### 5.2.1 Domain

The domain represents an idealized version of the geometry that is commonly observed seaward of an inlet, see Figure 5.2. A Cartesian coordinate system is adopted where the $x$-axis points seaward, the $y$-axis alongshore and the $z$-axis points upward. The position of the coastline is at $x = -x_s$. The coastline is interrupted by one inlet having a width $B$, typically in the order of 2 kilometers. At $x = 0$ the transition line from the surf zone to the inner shelf is located. It is assumed that there is hardly any interaction between the inner shelf and the surf zone. To avoid calculations in the surf zone, where the dynamics are very complicated and mainly driven by processes related to waves, the computational domain is at $x \in [0, \infty)$ and $y \in (-\infty, +\infty)$. In the regions far away from the inlet the water depth is assumed to be alongshore uniform with a constant depth $H_0$ at the coast and increasing exponentially to $H_s > H_0$ at the shelf break, i.e.

$$H_{\mathrm{R}}(x) = H_0 + (H_s - H_0)(1 - e^{-x/L}) \tag{5.1}$$

This depth profile was also used and motivated in Chapter 3 and in *van der Vegt et al.* (2005). Typical values for the depth parameters are $H_0 \sim 5$ m near the coast, $H_s \sim 25$ m far away from the inlet and an e-folding length scale of $L \sim 10$ km.
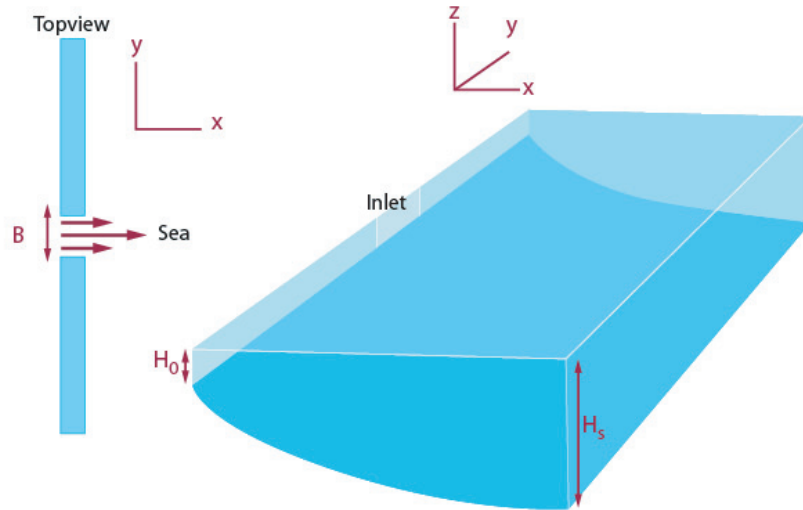


Figure 5.2: Schematic representation of the domain.

### 5.2.2 Hydrodynamics

**Waves**

The evolution and propagation of waves through the domain is described by the spectral action density balance (*Holthuijsen et al.*, 1989; *Booij et al.*, 1999, and references therein)

$$\frac{\partial N}{\partial t} + \frac{\partial (Nc_x)}{\partial x} + \frac{\partial (Nc_y)}{\partial y} + \frac{\partial (Nc_\omega)}{\partial \omega} + \frac{\partial (Nc_\theta)}{\partial \theta} = \frac{S}{\omega_*} \tag{5.2}$$

where $N$ is the spectral action density, defined as

$$N = \frac{E}{\omega_*} \qquad \omega_* = \omega - \vec{u} \cdot \vec{k} \tag{5.3}$$

Here, $E$ (in m²/Hz) is the variance per wave frequency and depends on the absolute frequency $\omega$ and wave direction $\theta$, as slowly varying functions of $x, y$ and time $t$. Furthermore, $\omega_*$ is the relative frequency of the waves, $\vec{u} = (u, v)$ is the depth-averaged current vector with components $u$ and $v$ in the $x$- and $y$-direction, respectively, and $\vec{k} = (k_x, k_y)$ is the wave vector with components $k_x$ and $k_y$ in the $x$- and $y$-direction, respectively. The relative frequency $\omega_*$ is the frequency observed while moving with the currents and the absolute frequency $\omega$ is the frequency of the wave observed by a stationary observer. The last term on the r.h.s. of Expression (5.3) represents the Doppler frequency shift. Here, weakly nonlinear waves are assumed. To a good approximation, they obey the dispersion relation

$$\omega_*^2 = gk \tanh(kD); \qquad k = |\vec{k}| \tag{5.4}$$

where $g = 9.81$ m²s⁻¹ is the acceleration due to gravity and $D = H+ < \zeta >$ is the total water depth. The water depth is composed of component $H$, which represents the position of the bottom with respect to $z = 0$, and of component $< \zeta >$, which represent the wave-averaged position of the sea level (due to tides and wave-induced set-up).

Furthermore, in Equation (5.2) the variables $c_x$ and $c_y$ are components of the vector $\vec{c} = \vec{c}_g + \vec{u}$, which is the propagation velocity of action density, with $\vec{c}_g = (\partial \omega_* / \partial k_x, \partial \omega_* / \partial k_y)$ is the intrinsic group velocity vector. The other variables in Equation (5.2) are defined as

$$c_\omega = \frac{\partial \omega_*}{\partial D} \frac{\partial D}{\partial t} + \vec{k} \cdot \frac{\partial \vec{u}}{\partial t} \qquad c_\theta = -\frac{1}{k} \frac{\partial \omega_*}{\partial D} \frac{\partial D}{\partial n} + \vec{k} \cdot \frac{\partial \vec{u}}{\partial n} \tag{5.5}$$

with $n$ a coordinate in the direction normal to the wave propagation.

The first term at the left-hand side of Equation (5.2) describes the time variation of the spectral energy density, the second and third term describe the divergence in the transport of action density by the group velocity and the currents. The fourth term describes the change in action density while moving in $\omega$-space and models the shift of the relative frequency due to variations in depth and currents. The fifth term describes a shift in action density while moving in $\theta$-space and models the effect of wave refraction by the bottom and the currents. The term on the right-hand side of Equation (5.2) includes the effects of generation of waves by wind, dissipation by white-capping, depth-induced breaking and bottom friction, and triad and quadruplet wave-wave interactions (*Holthuijsen et al.*, 1989; *Booij et al.*, 1999).

At the boundaries the spectral action is prescribed. A JONSWAP spectrum (*Hasselmann et al.*, 1973) is used and the characteristics of the incoming waves are characterized by four parameters: The significant wave height $h_{\text{sig}}$, the peak period $T_p$, the peak direction and the directional spreading. At the two other open boundaries the spectral action density is zero. At $x = 0$ it is required that wave energy leaves the domain (no reflection).

Interesting variables that come out of the model and are needed for the calculations of the currents and the sediment transport, are the amplitude of the near-bed wave orbital velocity $u_{orb}$, the wave-induced radiation stress tensor $\underline{S}$ and the mean peak value of the

bed-shear stress $\tau_w$ induced by the waves. Using results from linear wave theory it is found that

$$u_{orb} = \sqrt{\int \int \frac{2\omega^2}{\sinh^2(kD)} E(\omega, \theta) d\omega d\theta} \tag{5.6}$$

The time dependent near-bed wave-orbital vector is

$$\vec{u}_{\text{wave}} = \vec{u}_w \sin(\bar{\omega}t) \tag{5.7}$$

where $\bar{\omega}$ is the mean wave frequency and $\vec{u}_w$ is the magnitude and direction of the near-bed wave orbital motion:

$$\vec{u}_w = u_{orb} \begin{pmatrix} -\cos\bar{\theta} \\ \sin\bar{\theta} \end{pmatrix} \tag{5.8}$$

with $\bar{\theta}$ the mean direction of the waves with respect to the $y$-axis. The radiation stresses for random waves are defined as

$$\underline{S} = \begin{pmatrix} S_{xx} & S_{xy} \\ S_{yx} & S_{yy} \end{pmatrix}$$

with components

$$S_{xx} = \rho g \int \int [m \cos^2 \theta + m - \frac{1}{2}] E(\omega, \theta) d\omega d\theta \tag{5.9a}$$

$$S_{xy} = S_{yx} = \rho g \int \int m \sin \theta \cos \theta E(\omega, \theta) d\omega d\theta \tag{5.9b}$$

$$S_{yy} = \rho g \int \int [m \sin^2 \theta + m - \frac{1}{2}] E(\omega, \theta) d\omega d\theta \tag{5.9c}$$

where $m$ is the ratio of the group velocity and the phase velocity and $\rho$ the density of water. The peak value of the bed shear-stress due to waves ($\tau_w$) is defined as

$$\tau_w = \frac{1}{2} \rho f_w u_{orb}^2 \tag{5.10}$$

where

$$f_w = \begin{cases} 0.00251 e^{5.21(\frac{u_{orb}}{k_s \bar{\omega}})^{-0.19}} & ; \quad \frac{u_{orb}}{k_s \bar{\omega}} > \frac{\pi}{2} \\ \\ 0.3 & ; \quad \frac{u_{orb}}{k_s \bar{\omega}} < \frac{\pi}{2} \end{cases} \tag{5.11}$$

is the wave-induced friction stress factor that depends on the Nikuradse roughness length $k_s$ (typical value 1 mm) (see e.g. *Soulsby* (1997)).

## Currents

It is assumed that the currents have horizontal scales that are much larger than the vertical scale (typically kilometers versus meters) and that the vertical structure of the currents is not essential for the modeling of ebb-tidal deltas. The currents can therefore be described by the depth-averaged shallow water equations,

$$\frac{\partial \vec{u}}{\partial t} + (\vec{u} \cdot \vec{\nabla})\vec{u} = -g\vec{\nabla}\zeta - \frac{\vec{\tau_b}}{\rho D} - \frac{\vec{\nabla} \cdot \underline{S}}{\rho D} + A_h \nabla^2 \vec{u} \tag{5.12}$$

$$\frac{\partial \zeta}{\partial t} + \vec{\nabla} \cdot \left[ D\vec{u} \right] = 0 \tag{5.13}$$

which express the momentum and mass balance, respectively. In Equations (5.12) and (5.13) is $\vec{\nabla} = (\partial/\partial x, \partial/\partial y)$ the horizontal gradient vector, $\nabla^2$ the horizontal Laplace operator, $\zeta$ the sea surface elevation relative to the undisturbed water level $z = 0$, $\vec{\tau_b}$ the wave-averaged bed shear-stress vector and $A_h$ is the horizontal eddy viscosity coefficient.

The eddy viscosity coefficient is modeled as $A_h = lU_t$, with $l \sim 10$ m a mixing length scale and $U_t (\sim 1 \text{ ms}^{-1})$ a characteristic velocity scale related to the magnitude of the tidal currents. This formulation takes both small-scale turbulent eddies and vertical shear dispersion into account (*Zimmerman*, 1986). Following the model formulation of the idealized model described in Chapter 3, $U_t$ is defined as the maximum current amplitude in the tidal inlet,

$$U_t = MAX|\vec{u}(0,0,t)| \tag{5.14}$$

The radiation stresses $\underline{S}$ are output of the wave model (see Equation (5.2.2)) and may induce changes in mean sea level and wave-driven currents. The formulation of $\vec{\tau_b}$ is discussed in the next subsection.

To solve equations (5.12) and (5.13) boundary conditions are needed. At $x = 0$ outside the tidal inlet the shore-normal velocity is zero and a free slip condition is applied to have no exchange of momentum across the transition line. In the tidal inlet also a free slip condition is applied and the cross-shore velocity is prescribed as $u = \hat{U}(y,t)$, where $\hat{U}(y,t)$ is the given tidal velocity field in the inlet. The oscillating tidal flow in the inlet generates water motion in the entire domain. Far from the inlet the currents vanish.

## Bottom shear-stress formulations

In this study several formulations of the bottom shear-stress experienced by the currents are used. In experiments where waves are absent, two different formulations for $\vec{\tau_b}$ are considered. The first is

$$\vec{\tau_b} = \rho \frac{g}{C_z^2} |\vec{u}| \vec{u} \tag{5.15}$$

where $C_z$ is the Chézy coefficient and is set to its commonly used value $C_z = 65 \text{ m}^{1/2}\text{s}^{-1}$. This is the quadratic friction law. The second formulation reads

$$\vec{\tau_b} = \rho \frac{g}{C_z^2} \frac{8}{3\pi} U_t \vec{u} \tag{5.16}$$

Note that the stress in (5.16) is linear in the current. For this reason it will be referred to as the linearized bottom stress formulation. Using Equation (5.14) implies that in the center of the inlet the tidally averaged energy dissipation induced by the linearized bottom shear-stress (5.16) equals that of the full nonlinear stress (5.15) (*Lorentz*, 1922).

The third formulation for the bed shear-stress considers the case that both currents and waves are important constituents of the water motion. As is reviewed in *Soulsby et al.* (1993), all studies that deal with the wave-averaged bed shear-stress show that its magnitude increases when waves become stronger. This stress has a magnitude $\tau_b$ and is a function of two variables, $\tau_c$ and $\tau_w$. Here, $\tau_c$ is the magnitude of the current-induced bed shear-stress, of which the components are given in (5.15), and $\tau_w$ is the magnitude of the bed shear-stress induced by waves, as given by Equation (5.10). Both are quadratic in the velocity. The direction of the stress, $\beta$, is in general different from that of the waves and the currents. In the present model the formulations for $\tau_b$ and direction $\beta$ as proposed by *Fredsøe* (1984) are used.

## 5.2.3   Sediment transport

For the sediment transport the formulation of *van der Vegt et al.* (2005), as described in Section 3.2.3, is used. This is a generalized Bagnold-Bailard formulation (*Bagnold*, 1966; *Bailard*, 1981). The sediment is transported as bedload. A correction for the direction of the sediment transport is introduced that accounts for the influence of the bed slope. Furthermore, the bedload transport is averaged over the wave and tidal period. This yields

$$\vec{q} = \vec{q}_f + \vec{q}_{\text{bot}} + \vec{q}_{\text{asym}} \tag{5.17}$$

where $< \cdot >$ denotes an averaging over the tidal period of the variable within the brackets. In Equation (5.17) is $\vec{q}_f$ the tidally averaged sediment transport induced by the waves and currents, $\vec{q}_{\text{bot}}$ induced by bed slope effects and $\vec{q}_{\text{asym}}$ induced by nonlinear effects of waves. The sediment transport relation is defined at the top of the wave boundary layer. Because the tidal currents are depth-averaged, the depth-averaged currents are transformed to their magnitudes at the top of the wave boundary layer by assuming a logarithmic velocity profile. The sediment transport due to waves and currents is expressed as

$$\vec{q}_f = \alpha\beta^3 < |\vec{u}|^2\vec{u} + \frac{1}{2}\frac{|\vec{u}_w|^2}{\beta^2}\vec{u} + (\vec{u} \cdot \frac{\vec{u}_w}{\beta})\frac{\vec{u}_w}{\beta} > \tag{5.18}$$

with $\alpha$ a grain size dependent constant (typical value of $10^{-5}$ s$^2$m$^{-1}$) and $\beta \sim 0.35$ a factor that relates the tidal currents at the top of the wave boundary layer to the depth-averaged tidal currents. Here, $\beta$ is assumed to be constant in the domain while in reality it will be a weakly varying function of the local water depth. Note that $\vec{q}_f = 0$ in the absence of tidal currents. The mean sediment transport due to the presence of bed slopes reads

$$\vec{q}_{\text{bot}} = \alpha\beta^p\gamma U^p\vec{\nabla}H \tag{5.19}$$

In this expression $U$ is the magnitude of the flow due to waves and currents and is defined as

$$U = \sqrt{U_t^2 + (u_{orb}/\beta)^2} \tag{5.20}$$

Furthermore, in Equation (5.19) is $\gamma$ the bed-slope coefficient (with a typical value of $1(\frac{m}{s})^{3-p}$). The constant $p$ is determined from observations and is found to be $p = 2$ (*Struiksma et al.*, 1985) or $p = 3$ (*Bailard*, 1981; *Sekine and Parker*, 1992). In this study $p = 2$. The last term of Equation (5.17) is the sediment transport due to nonlinear effects of waves (wave asymmetry). It reads

$$\vec{q}_{\text{asym}} = -\alpha\gamma\beta^2 U^2 \vec{\nabla} H_{\text{R}} \tag{5.21}$$

where $H_{\text{R}}$ is defined in Equation (5.1). The sediment transport $\vec{q}_{\text{asym}}$ is chosen such that it balances the off-shore sediment transport induced by the bed slopes when tidal currents through the inlet are zero. For further details, see Chapter 3.

For further use, $\vec{q}_f$ is considered in more detail. Assume that $\vec{u} =< \vec{u} > +\vec{u}'$, i.e., the currents are composed of a residual and a time-varying (tidal) component. In that case $\vec{q}_f$ can be split into

$$\vec{q}_f = \vec{q}_{\text{res}} + \vec{q}_a + \vec{q}_{\text{wave}} \tag{5.22}$$

where $\vec{q}_{\text{res}}$ is that part of the flow-induced sediment transport that involves residual and tidal currents, $\vec{q}_a$ only depends on $\vec{u}'$ and is related to tidal asymmetry (*van de Kreeke and Robaczewska*, 1993) and $\vec{q}_{\text{wave}}$ involves sediment transport due to waves and residual currents. The components read

$$\vec{q}_{\text{res}} = \alpha\beta^3[(| < \vec{u} > |^2 + < |\vec{u}'|^2 >) < \vec{u} > + < (\vec{u}' \cdot < \vec{u} >)\vec{u}' >] \tag{5.23a}$$

$$\vec{q}_a = \alpha\beta^3 < |\vec{u}'|^2 \vec{u}' > \tag{5.23b}$$

$$\vec{q}_{\text{wave}} = \alpha\beta^3 [\frac{|\vec{u}_w|^2}{2\beta^2} < \vec{u} > + \frac{\vec{u}_w \cdot < \vec{u} >}{\beta^2} \vec{u}_w] \tag{5.23c}$$

### 5.2.4 Sediment mass balance

At locations where the sediment transport is divergent (convergent) the water depth will increase (decrease). The behavior of the water depth in time is governed by the bed evolution equation

$$\frac{\partial H}{\partial t} - \vec{\nabla} \cdot \vec{q} = 0 \tag{5.24}$$

The bottom only changes due to divergences and convergences in the tidally averaged sediment transport. This can be used because the time scale on which bottom patterns evolve (typically in the order of years) is much larger than the time scale of the currents ($M_2$ period). This implies that the bottom hardly changes during the calculation of the currents and waves and can be taken as a constant (*Sanders and Verhulst*, 1985). The boundary conditions for the sediment mass balance are that far from the inlet the mean sediment transport vanishes. At $x = 0$ outside the inlet the mean cross-shore sediment flux is zero. In the tidal inlet a regularity condition for the depth is imposed ($H$=finite).

### 5.2.5   Morphodynamic equilibrium

In this study the focus is on morphodynamic equilibria. These are defined as states which involve a bottom that does not change in time,

$$\frac{\partial H}{\partial t} = 0 \tag{5.25}$$

Henceforth $H$ will represent an equilibrium bathymetry. In morphodynamic equilibrium currents and waves are still present and transport sediment. Note that Equations (5.25) and (5.24) imply that in equilibrium the net sand transport is non-divergent

$$\vec{\nabla} \cdot \vec{q} = 0 \tag{5.26}$$

## 5.3   Methods

### 5.3.1   Domain

The model equations have to be solved on a finite domain. This domain is designed such that it represents the infinite domain as described in Section 5.2.1. A finite rectangular domain is chosen which is centered around the tidal inlet and has a length $2L_y$ in the alongshore direction and $L_x$ in the cross-shore direction. The domain is chosen large enough to have vanishing velocities at the seaward boundaries.

### 5.3.2   Hydrodynamics

**Waves**

To solve the wave model as described in Section 5.2.2 a state-of-the-art numerical model is used, called SWAN. The model variables are calculated on a numerical grid. The domain is divided into $N_y^w$ and $N_x^w$ grid points in the $y$- and $x$-direction, respectively. At one seaward boundary (at $x = L_x$) the wave characteristics are prescribed. At the other boundaries full absorbtion of wave energy is assumed. A detailed description of SWAN and the numerical details can be found in *Booij et al.* (1999).

**Currents**

To solve the shallow water equations the hydrodynamic module of Delft3D is used. Delft3D is a process-oriented numerical model developed by WL-Delft Hydraulics. In this study the 2D (depth-averaged) version is used. The domain that is used in the calculations is the same as the domain that is used for the calculations of the waves. The number of grid points $(N_x^c, N_y^c)$, however, is larger than in the wave model. At $x = 0$ a closed wall is used, except for one region with width $B$ that models the tidal inlet. At the closed boundary the cross-shore velocity is zero and a free slip condition is applied. In the inlet a discharge boundary is used in which the cross-shore velocity is prescribed. By using this discharge boundary no free-slip condition in the inlet can be applied. Instead, during ebb (outflow) the tangential advection is neglected ($v\partial u/\partial y = 0, v\partial v/\partial y = 0$).

During flood no extra boundary condition is required. For numerical details on Delft3D, see *Stelling and Leendertse* (1992); *Roelvink and van Banning* (1994).

### 5.3.3  Sediment transport

In the idealized model higher harmonics of the tide were not accounted for. Since the first goal is to validate and compare the results of the idealized model with the results that are obtained with the numerical model, two cases are considered in this study. In the first case the time series of $\vec{u}$ is decomposed into a Fourier series. This series is truncated after the $M_2$ component. With this truncated series of the velocity the sediment transport due to tides ($\vec{q}_f$) is calculated. This equals the formulation of $\vec{q}_f$ as is used in the idealized model (Equation (3.15) of Chapter 3). It will be referred to as $\vec{q}_{fM_0M_2}$. Note that $\vec{q}_a = 0$ in this case. In the second case the complete time series of $\vec{u}$ is used to calculate $\vec{q}_f$.

### 5.3.4  Morphodynamic equilibria

**Mathematical description**

A continuation method is used to obtain morphodynamic equilibria. This method requires a known equilibrium solution to start from. In the present model the latter corresponds to the situation that there are no tidal currents and $H = H_{\mathrm{R}}(x)$. In that case the divergence of the sediment transport due to bed slopes balances the divergence of the sediment transport due to wave asymmetry. When currents through the tidal inlet are nonzero the following balance holds:

$$\alpha\beta^2\gamma U^2\nabla^2 H' = -\vec{\nabla}\cdot\vec{q}_f \tag{5.27}$$

where $H' = H - H_{\mathrm{R}}$. This balance is obtained by substituting Equation (5.17) and Equation (5.19) into Equation (5.26) and using the sediment mass balance in case that tidal currents through the inlet are zero. Because $\vec{q}_f$ is an implicit function of $H'$, Equation (5.27) describes a nonlinear differential equation for $H'$. The boundary conditions are that at the seaward boundaries the mean sediment transport vanishes. At $x = 0$ outside the inlet the cross-shore component of the sediment transport is zero. Using the definition of $\vec{q}_{\mathrm{asym}}$ (Equation (5.21)) and that the cross-shore component of $\vec{q}_f$ is zero, this yields that $\partial H'/\partial x = 0$. Inside the inlet a regularity condition for $H'$ is applied.

**Continuation method and iteration procedure**

A schematic representation of the method to calculate morphodynamic equilibria is shown in Figure 5.3. Starting point is a known equilibrium solution of the model. The corresponding bottom pattern is denoted by $H = H(x, y; \mu)$, where $\mu$ represents a parameter (e.g., the typical velocity scale in the center of the inlet $U$). Next, the parameter $\mu$ is changed by a small increment $\Delta\mu$. As long as the increment is small enough, it can be assumed that $H = H(x, y; \mu + \Delta\mu)$ does not differ much from $H = H(x, y; \mu)$. To solve

Equation (5.27) an iterative procedure is used. The previous estimate of the morphodynamic equilibrium is used to calculate the waves and currents. From this, $\vec{q}_f$ and $\vec{\nabla} \cdot \vec{q}_f$ are calculated and the right-hand side of Equation (5.27) is known. This equation has now become a Poisson equation which is subsequently solved by using a multipole expansion in the elliptic-cylindrical coordinates. A detailed description of this coordinate system and how the Poisson problem is solved can be found in Chapter 3. If the new bathymetry differs much from the previous estimate, a new iteration is performed. This procedure is repeated until convergence is established and the morphodynamic equilibrium for the parameter setting is obtained. From this, the parameter $\mu$ can be changed again.
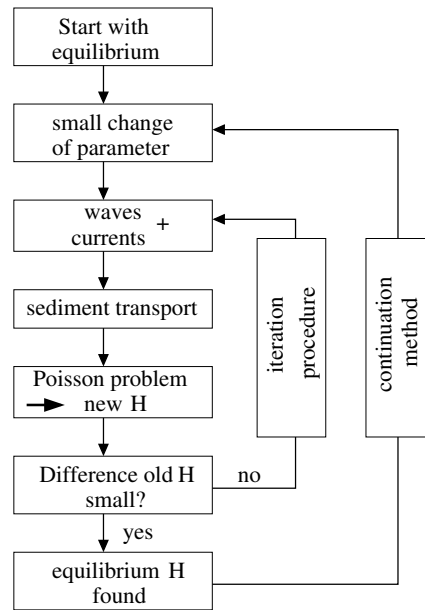


Figure 5.3: Schematic representation of the iteration procedure and continuation method. Further details are given in the text.

## 5.4 Results

### 5.4.1 Set-up of the experiments

The default model set-up is chosen such that it is as close as possible to that of the idealized model. This means that a linearized bed shear-stress formulation is used, no waves are considered and $\vec{q}_f = \vec{q}_{fM_0M_2}$. Next, the sensitivity of the results to extensions of the model formulation are studied. An overview of all the experiments and in which section the results are presented is given in Table 5.1.

The numerical parameters that are used for the experiments are shown in Table 5.2. The domain covers the area from $x \in [0, 15]$ km and $y \in [-15, 15]$ km. Test experiments showed that this choice of the domain obeys the condition of vanishing velocity far away from the inlet. The total area spanned is 15 x 30 km and is divided into $N_x^c = 150$ and $N_y^c = 300$ grid points in $x$- and $y$-direction, respectively. The grid distance $\Delta x = 100$

| Section | Bed shear-stress | Higher harmonics | Sediment transport | Waves |
|---------|------------------|------------------|--------------------|-------|
| 4.2 + 4.3 | Linear | No | $\vec{q}_f = \vec{q}_{fM_0M_2}$ | No |
| 4.4.1 | Linear | Internal | $\vec{q}_f = \vec{q}_{\text{res}} + \vec{q}_a$ | No |
| 4.4.2 | Linear | Internal + External | $\vec{q}_f = \vec{q}_{\text{res}} + \vec{q}_a$ | No |
| 4.5 | Quadratic | Internal | $\vec{q}_f = \vec{q}_{\text{res}} + \vec{q}_a$ | No |
| 4.6 | *Fredsøe* (1984) | Internal | $\vec{q}_f = \vec{q}_{\text{res}} + \vec{q}_a + \vec{q}_{\text{wave}}$ | Yes |

Table 5.1: Overview of the experiments performed in this study.

m and $\Delta y = 100$ m is found from convergence tests as the optimum choice when both considering accuracy and calculation time. The numerical time-step used is $\Delta t = 2$ minutes and the total simulation time is four tidal periods. Only the fourth tidal period is used for the sediment transport calculations. Test experiments showed that the transients were damped after three periods. To solve the wave model a coarser grid is used. The grid distance is 300 m and $N_x^w = 50$ and $N_y^w = 100$. The wave parameters that are calculated on the grid for the waves are linearly interpolated to the grid of the currents. The number of poles that are used to solve the Poisson problem is 150.

| Parameter | Delft3D | SWAN |
|-----------|---------|------|
| $L_x$ | 15 km | 15 km |
| $L_y$ | 15 km | 15 km |
| $\Delta x$ | 100 m | 300 m |
| $N_x$ | 150 | 50 |
| $\Delta y$ | 100 m | 300 m |
| $N_y$ | 300 | 100 |
| $\Delta t$ | 120 s | |

Table 5.2: Numerical parameters of SWAN and Delft3D as used in the calculations.

### 5.4.2 Results for default case

In the default case $B = 2$ km. The cross-shore bottom profile is described by Equation (5.1), with $H_0 = 5$ m at the coast, $H_s = 25$ m and an e-folding length scale of $L = 10$ km. These values are characteristic for the reference bathymetry observed along the barrier coast of the US (see Chapter 3). The forcing of the water motion is due to the tidal current in the inlet (no waves). The current profile over the inlet is equal to the one used in Chapter 3 and only an $M_2$ tidal component is prescribed:

$$\hat{U}(y,t) = U_{M_2}[(2\frac{y}{B} - 1)^3(2\frac{y}{B} + 1)^3]\cos(\sigma t) \tag{5.28}$$

Here, $\sigma = 1.4 \cdot 10^{-4}$ s$^{-1}$ denotes the frequency of the $M_2$ tide. The profile is symmetric with respect to the mid-axis of the inlet and the velocity amplitude increases from zero on both sides ($y = \pm B/2$) to a maximum value in the middle ($y = 0$). The typical velocity

scale $U$, needed to calculate the linearized bottom stress and the sediment transport, and the velocity scale $U_t$ to calculate the eddy viscosity coefficient $A_h$, become $U = U_t = U_{M_2}$. In this experiment $U_{M_2} = 0.2$ ms$^{-1}$. In Table 5.3 the values of the model parameters for this default experiment are given.

| Parameter | Choice |
|:---------:|:------:|
| $B$ | 2 km |
| $H_0$ | 5 m |
| $H_s$ | 25 m |
| $L$ | 10 km |
| $\hat{U}$ | Eq. (5.28) |
| $U$ | $U_{M_2}$ |
| $U_t$ | $U_{M_2}$ |
| $U_{M_2}$ | 0.2 ms$^{-1}$ |
| $C_z$ | 65 m$^{1/2}$s$^{-1}$ |
| $A_h$ | 2.8 m$^2$s$^{-1}$ |
| $\alpha$ | $10^{-5}$ s$^2$m$^{-1}$ |
| $\gamma/\beta$ | $1(\frac{m}{s})$ |
| $p$ | 2 |

Table 5.3: Parameter values for the default experiment.

Within the iteration procedure the first estimate of the equilibrium bathymetry for $U_{M_2} = 0.2$ ms$^{-1}$ is $H = H_R(x)$. The velocity pattern at two phases of the tide and the residual current pattern are shown in Figure 5.4; Figure 5.4(a) shows the currents at maximum ebb and Figure 5.4(b) at maximum flood. During ebb the water mainly flows in the cross-shore direction. The alongshore velocity components are small. This resembles an ebb-jet. During the flood phase the water flows from all sides towards the inlet. The alongshore component of the velocity almost has the same magnitude as its cross-shore component. The residual velocity pattern is shown in Figure 5.4(c). It reveals the presence of two counter-rotating residual circulation cells at some distance from the inlet. The maximum of the residual currents is 0.03 ms$^{-1}$.

The net sediment transport $\vec{q}_{fM_0M_2}$ is shown in Figure 5.5(a). The sediment is transported from the sides towards the inlet. From the inlet the sediment is transported seaward. The convergence of the net sediment transport is shown in Figure 5.5(b). It yields negative values near the inlet and positive values further seaward.

From this convergence the new estimate for $H$ is calculated and is shown in Figure 5.6(a). It reveals a channel-shoal pattern. In the center of the inlet a channel is found and at its end a shoal is located, the ebb-tidal delta. This shoal is flanked by two smaller channels. Because this bathymetry differs much ($\sim 1.5$ m) from the old bathymetry, a next iteration is needed. The new bathymetry gives rise to changes in the currents and net sediment transport and repetition of the procedure results in a new guess for the bathymetry, etc. The bottom changes appear to be gradual with decreasing differences between the successive estimates of $H$. After 7 iterations the maximum difference with the previous estimate is less than 4 cm and equilibrium is reached. This bathymetry is shown in Figure

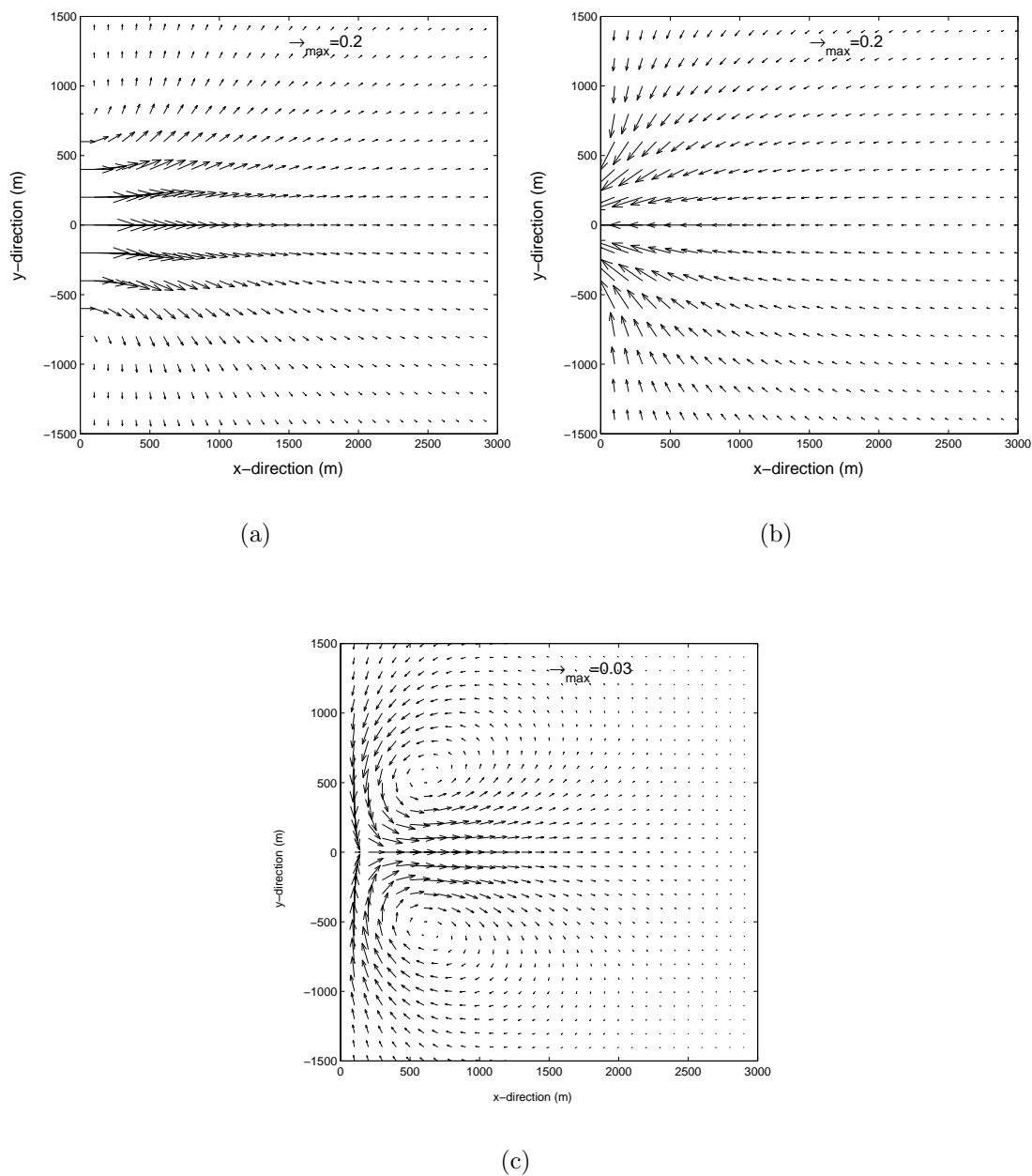(a)                                                                    (b)



(c)

Figure 5.4: (a) The velocity field during ebb in the default experiment, first iteration step. For model setting and parameter values, see Tables 5.1-5.3. The inlet is located at $(x, y) = (0, 0)$ and has a width $B = 2$ km. (b) Same as (a), but now during flood. (c) Vector plot of the residual currents

5.6(b). Clearly, a shoal is found seaward of the inlet with its center around $x = 1000$ m. This shoal resembles an ebb-tidal delta. The depth above the shoal is 1 m smaller than the depth of the reference bathymetry at that position. Furthermore, a channel in the inlet is modeled which is about 1.5 m deeper than the reference bathymetry at this position. It is an ebb-dominated channel. The two channels that flank the delta are flood-dominated
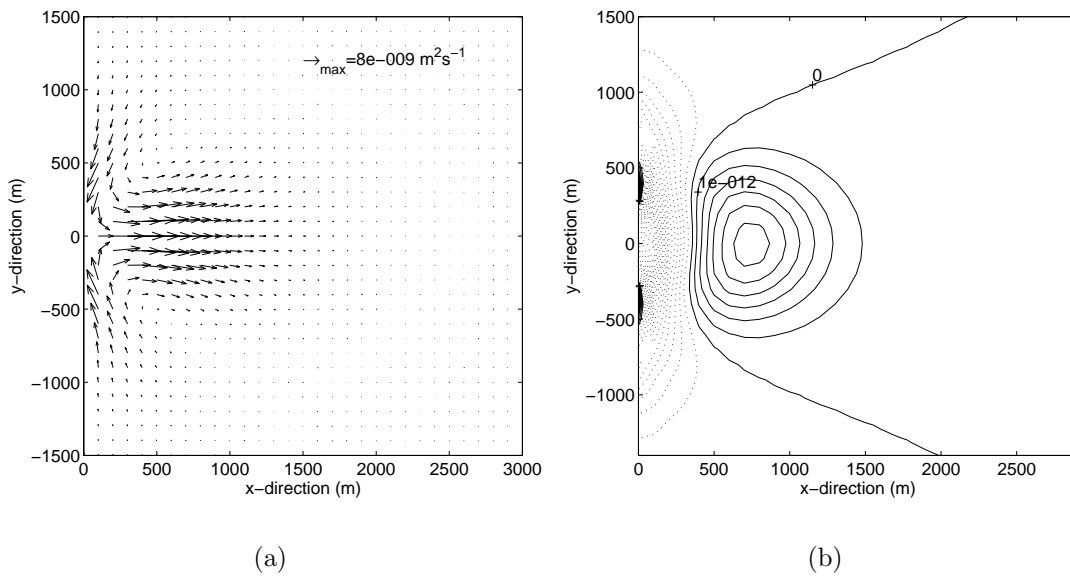
(a)                                                                                                          (b)

Figure 5.5: Variables at the first iteration step in the default experiment when $H = H_{\mathrm{R}}(x)$.
(a) Mean sediment transport $\vec{q}_{fM_0M_2}$. (b) Convergence of mean sediment transport, $-\vec{\nabla} \cdot \vec{q}_{fM_0M_2}$.
Contour intervals are $1 \cdot 10^{-12}$ ms$^{-1}$.

channels. The presence of the inlet is still noticeable at 3 km away from the inlet by the
curving of the isobaths.



(a)                                                                                                          (b)
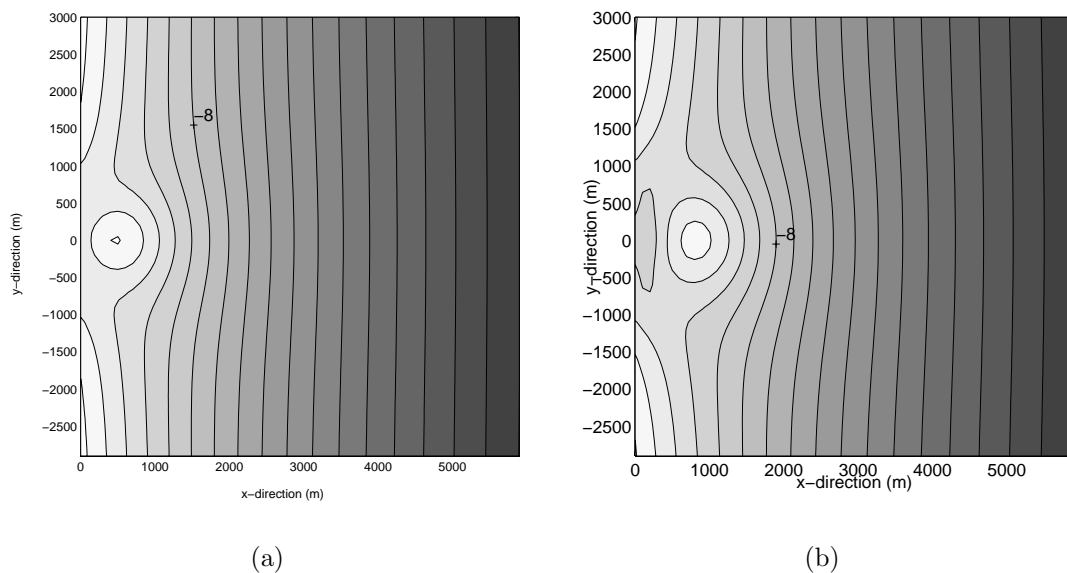
Figure 5.6:   (a) Estimate of equilibrium bathymetry after first iteration step. Contour intervals
are 0.5 meter. (b) Equilibrium bathymetry for the default experiment. For model setting and
parameter values, see Tables 5.1-5.3. Contour lines are drawn every 0.5 m.

### 5.4.3 Sensitivity of model results to tidal velocity amplitude in the inlet

A series of experiments has been performed for different values of $U_{M_2}$. Other parameter values were identical to those used in the default experiment. Because the procedure to obtain morphodynamic equilibrium and the resulting patterns for currents and sediment transport are similar to those of the default experiment, only the equilibrium bathymetries are presented. They are shown in Figure 5.7.

With increasing amplitude of the tidal current the channel-shoal pattern becomes more pronounced. An increase of $U_{M_2}$ results in an increase of the depth of the channels and a shift of the delta in the seaward direction. For $U_{M_2} = 0.10$ ms$^{-1}$ the shoal is 0.4 m above the reference bathymetry $H_{\mathrm{R}}$, for $U_{M_2} = 0.30$ ms$^{-1}$ this is $\sim$2 m. For $U_{M_2} = 0.10$ ms$^{-1}$ the depth in the channel is 0.5 m beneath the reference bathymetry, for $U_{M_2} = 0.30$ ms$^{-1}$ this is $\sim$3 m. For $U_{M_2} > 0.30$ ms$^{-1}$ no equilibrium solutions are found. This will be discussed in Section 5.7.

### 5.4.4 Sensitivity of results to tidal asymmetry

In the previous experiments the sediment transport is calculated with only the $M_0$ and $M_2$ components of the tide. Although being the dominant constituents, higher harmonics of the tide are present as well. The effect of these higher harmonics on the results is studied by a series of experiments in which $\vec{q}_f = \vec{q}_{\mathrm{res}} + \vec{q}_a$ instead of $\vec{q}_f = \vec{q}_{fM_0M_2}$. So, $\vec{q}_a$ is nonzero and $\vec{q}_{\mathrm{res}}$ also includes effects of the higher harmonics of the tide, see Equations (5.23a) and (5.23b). Two cases are considered. In the first case, only the internally generated higher harmonics of the tide are considered, i.e., higher harmonics that are generated by nonlinear processes. In the second case, also externally generated higher harmonics are considered by imposing an $M_4$ component on the prescribed cross-shore tidal currents in the inlet.

**Internally generated higher harmonics**

The same parameter setting as in the default experiment is used. At the first iteration the current patterns during maximum ebb and flood and the residual current pattern are identical to the default experiment. After decomposing the velocity components into its Fourier components it is found that the maximum magnitude of long axis of the $M_4$ tidal current ellipse is 0.013 ms$^{-1}$, or about 6 % of the $M_2$ tidal current amplitude. The tidal current ellipses of the $M_4$ tide are shown in Figure 5.8(a). The pattern consists of two cells. In the center of the inlet the $M_4$ current ellipses are bidirectional, while at the sides there is stronger ellipticity. The magnitude of the $M_6$ tidal currents is much smaller than the $M_4$ tidal currents, with a maximum magnitude of the long axis of the $M_6$ tide of 0.002 ms$^{-1}$. The residual sediment transport $\vec{q}_{\mathrm{res}}$ is almost equal to $\vec{q}_{fM_0M_2}$ in the default case and is therefore not shown. In Figure 5.8(b) $\vec{q}_a$ is shown and its convergence is shown in Figure 5.9(a). The sediment transport due to the higher harmonics of the tide has a similar pattern as $\vec{q}_{\mathrm{res}}$. However, the magnitudes of $\vec{q}_a$ are 10 times smaller than those of $\vec{q}_{\mathrm{res}}$. The convergence of $\vec{q}_a$ has a similar pattern as the convergence of $\vec{q}_{\mathrm{res}}$, but they are a
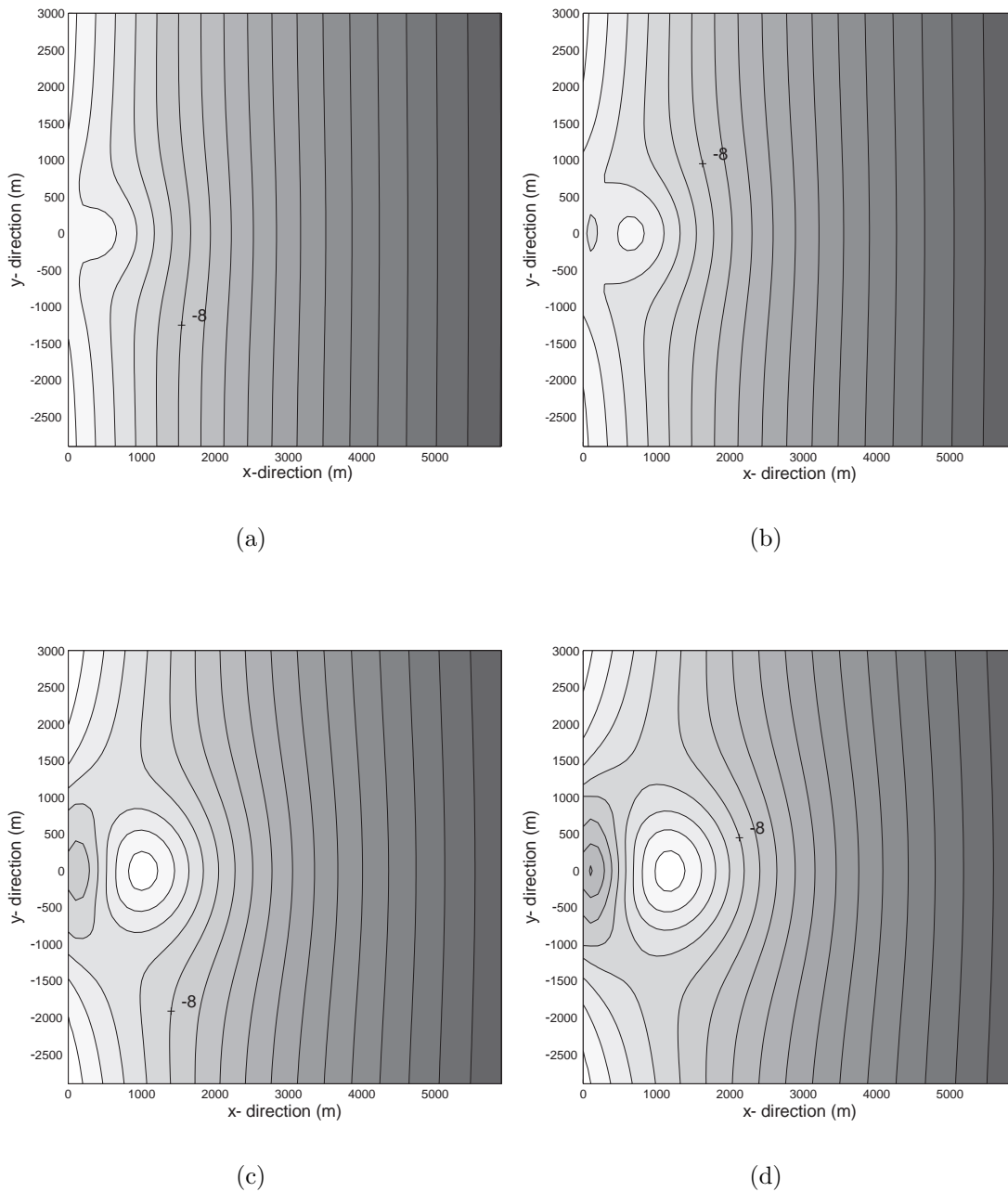
(a)



(b)



(c)



(d)

Figure 5.7: Equilibrium bathymetries for different values of $U_{M_2}$. Contour lines every 0.5 meter. For model setting and parameter values, see Tables 5.1-5.3. Note that $A_h$ and $U$ increase if $U_{M_2}$ increases. (a) $U_{M_2} = 0.1$ ms$^{-1}$ ; (b) $U_{M_2} = 0.15$ ms$^{-1}$; (c) $U_{M_2} = 0.25$ ms$^{-1}$; (d) $U_{M_2} = 0.30$ ms$^{-1}$.

factor 10 smaller. The initial erosion-deposition rate is increased by about 10 % compared to the default experiment. From the convergence in the sediment transport a new estimate of the equilibrium bathymetry is calculated. After a few iterations equilibrium is reached. The modeled equilibrium bathymetry is shown in Figure 5.9(b). It only differs slightly

from that of the default experiment (Figure 5.6(b)). It is characterized by a slightly deeper channel near the inlet and a shoal that extends a bit further in the alongshore direction. These results indicate that internally generated nonlinear overtides hardly affect the main characteristics of the ebb-tidal delta.
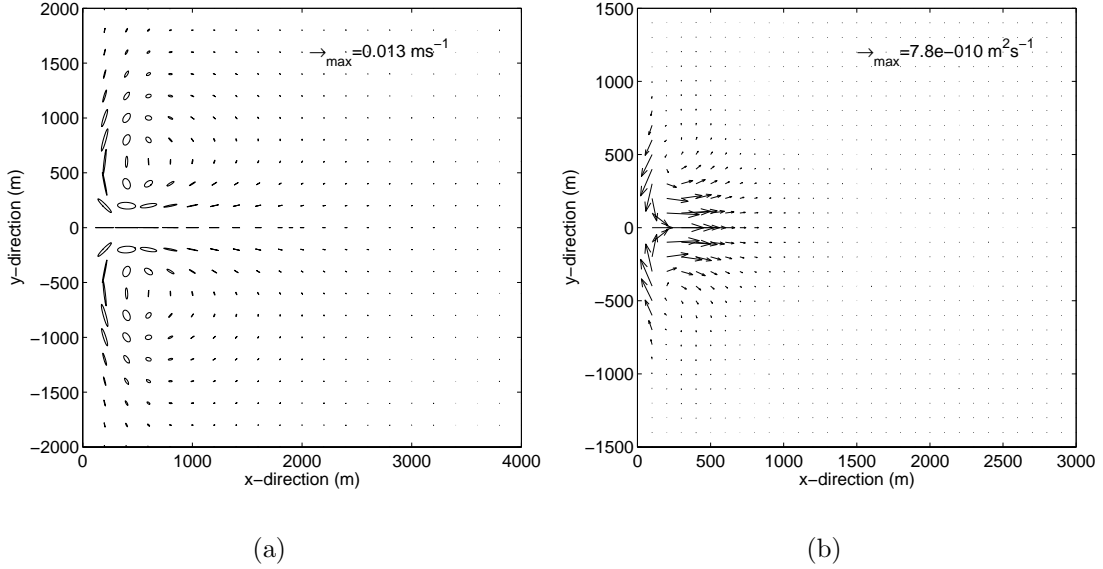


(a)                                                       (b)

Figure 5.8:   (a) Current ellipses of $M_4$ tide at the first iteration step in the experiment with internally generated higher harmonics. For model setting and parameter values, see Tables 5.1-5.3. (b) $\vec{q}_a$ at the first iteration step.

**Externally prescribed higher harmonics**

In the experiments described in this section an external higher harmonic constituent is prescribed in the inlet. The cross-shore velocity component in the tidal inlet is specified as

$$\hat{U}(y,t) = U_{M_2}[(2\frac{y}{B} - 1)^3(2\frac{y}{B} + 1)^3][\cos(\sigma t) + \frac{U_{M_4}}{U_{M_2}}\cos(2\sigma t - \phi)] \qquad (5.29)$$

with $U_{M_4}$ the magnitude of the $M_4$ tidal currents and $\phi$ the relative phase between the $M_2$ and $M_4$ tidal currents. For $\phi = 0°$ the current in the inlet is ebb-dominated, for $\phi = 90°$ there is no dominance (peak flood currents equals peak ebb currents) and for $\phi = 180°$ the current in the inlet is flood-dominated. Observations show that the velocity in the inlet can have a large $M_4$ component. For instance, Price Inlet in South Carolina is ebb-dominated and $U_{M_4}/U_{M_2} = 0.16$ (*FitzGerald and Nummedal*, 1983). Here, results are presented of experiment in which a relatively strong external $M_4$ is prescribed with $U_{M_4} = 0.0375$ ms$^{-1}$, $U_{M_2} = 0.15$ ms$^{-1}$ and $\phi = 0°, 90°$ or $180°$. Note that the value of $U$, which is defined in Equation (5.14), now depends on $\phi$. For $\phi = 0°$ and $\phi = 180°$ $U = 0.1875$ ms$^{-1}$, while for $\phi = 90°$ $U = 0.165$ ms$^{-1}$. All other parameters have their

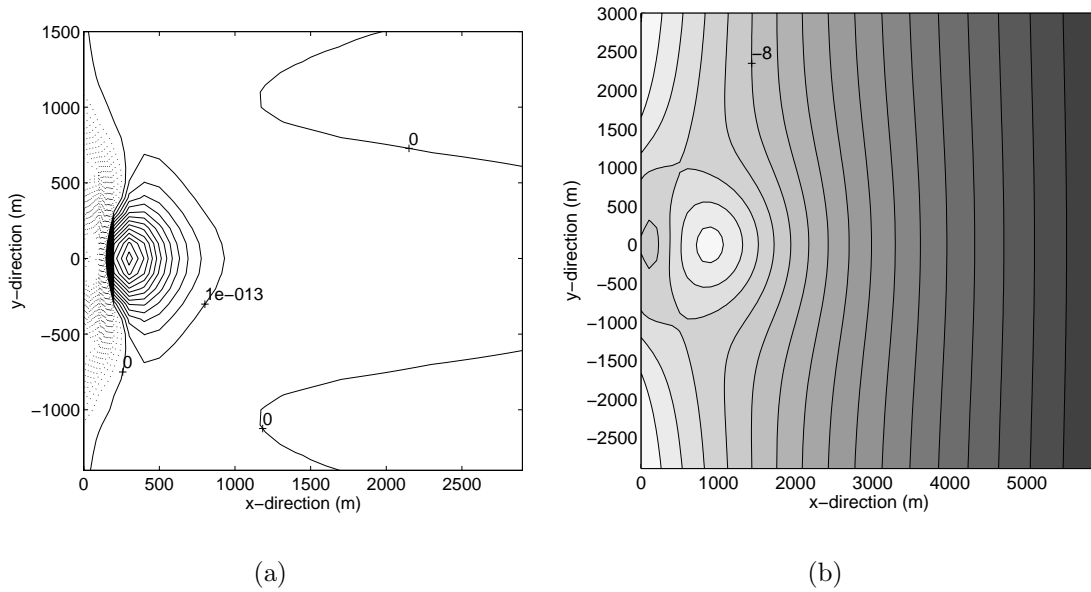(a)                                                                    (b)

Figure 5.9: (a) Convergence of $\vec{q}_a$ at the first iteration step. Contour lines are drawn every $10^{-13}$ ms$^{-1}$. (b) The equilibrium bathymetry in the experiment with internally generated higher harmonics. Contour lines every 0.5 meter.

default values. Furthermore, $\vec{q}_f = \vec{q}_{\mathrm{res}} + \vec{q}_a$ and is calculated with Equations (5.23a) and (5.23b).

For these three cases morphodynamic equilibrium has been calculated. The tidal current pattern during maximum ebb in morphodynamic equilibrium are almost similar for the three cases. For $\phi = 0°$, $\phi = 90°$ and $\phi = 180°$ the flow pattern during maximum ebb resembles an ebb-jet. However, the maximum magnitudes of the currents are relatively large for $\phi = 0°$ (0.19 ms$^{-1}$), moderate for $\phi = 90°$ (0.165 ms$^{-1}$) and relatively weak for $\phi = 180°$ (0.11 ms$^{-1}$). The magnitudes of the residual currents in equilibrium are different for the various phases. In case of ebb-dominated currents, the residual currents are largest. When the inlet is flood-dominated the residual currents are weakest. The tidal current ellipses of the $M_4$ tide are similar for various phases $\phi$. The ellipses are mainly bidirectional.

In the case that $\phi = 0°$ the presence of higher harmonics of the tide results in a nonzero $\vec{q}_a$. The sediment is removed from the center of the inlet and transported in the seaward direction. The convergence of $\vec{q}_a$ results in positive values (deposition) in the whole domain and the magnitudes are much larger than those obtained in the experiment with internally generated higher harmonics. In morphodynamic equilibrium the divergence of the flow-induced sediment transport is balanced by $\vec{\nabla} \cdot \vec{q}_{\mathrm{bot}}$. The equilibrium bathymetry is shown in Figure 5.10(a). The channel-shoal pattern is more pronounced than in the default experiment (compare with Figure 5.6(b)). The channel is more extended in the alongshore direction.

In the case that $\phi = 90°$ the sediment transport $\vec{q}_s$ has an almost similar pattern as in the experiment with internally generated higher harmonics (Figure 5.8(b)). However, the

magnitudes are larger. The convergence of the sediment transport has a similar pattern as the pattern of $-\vec{\nabla} \cdot \vec{q}_{\text{res}}$. The channel-shoal pattern of the equilibrium bathymetry is similar to the situation that no external $M_4$ is prescribed in the inlet as is shown in Figure 5.10(b).

In the case that $\phi = 180°$ the currents in the inlet are flood-dominated. The sediment transport due to the higher harmonics of the tide ($\vec{q}_a$) results in a transport of sediment from all sides towards the inlet. The convergence of $\vec{q}_a$ causes a strong erosion in the entire domain and dominates the erosion and deposition pattern induced by $\vec{\nabla} \cdot \vec{q}_{\text{res}}$. The equilibrium bathymetry is shown in Figure 5.10(c). It has a completely different channel-shoal pattern compared to the previous experiments. The equilibrium bathymetry for $\phi = 180°$ is characterized by a channel near the center of the inlet and on both sides a delta.

### 5.4.5 Sensitivity of results to quadratic bottom stress

In the experiments described in this section a quadratic bottom stress formulation is used instead of the linearized one. No waves are considered. The sediment transport calculations include the effect of the higher harmonics of the tide and is calculated with Equations (5.23a) and (5.23b), where $\vec{u}$ contains all tidal harmonics. All other parameters have their default values (Table 5.3).

Figure 5.11(a) shows the residual currents and sediment transport at the first iteration step. The residual currents are stronger than those obtained in the default experiment (compare with Figure 5.5), typically 0.05 ms$^{-1}$ versus 0.03 ms$^{-1}$. In addition, the spatial extensions of the residual circulation cells in Figure 5.11(a) are larger than those of the default experiment. The center of the cells is at $(x, y) = (1000, \pm 800)$, where in the default experiment they are at $(x, y) = (600, \pm 600)$. A vector plot of the sediment transport $\vec{q}_f$ is shown in Figure 5.11(b). The sediment is transported from the sides of the inlet towards the center. From the center of the inlet the sediment is transported in the seaward direction. The convergence of $\vec{q}_f$ in equilibrium is shown in Figure 5.12(a). Interestingly, the convergence of the sediment transport shows a first indication that the delta tends to fold around the channel. The area with positive values folds around the area with negative values. The equilibrium bathymetry is shown in Figure 5.12(b). The modeled channel-shoal pattern is more pronounced compared to that of the default experiment ( Figure 5.6(b)). The delta protrudes about 2 km into the sea and extends further in the alongshore direction. The height of the delta is almost the same as the delta in the default experiment. The channel in the center of the tidal inlet is deeper than in the default case.

Additional experiments were performed in which $U_{M_2}$ is varied. For each experiment the position of the shoal has been determined. Increasing the tidal current amplitude results in a seaward shift of the position of the shoal (Figure 5.13). The maximum depth of the channel increases with increasing $U_{M_2}$.

### 5.4.6 Sensitivity of results to waves

In the experiment described in this section the water motion is forced by both cross-shore tidal currents in the inlet and by waves of which the characteristics are imposed at the
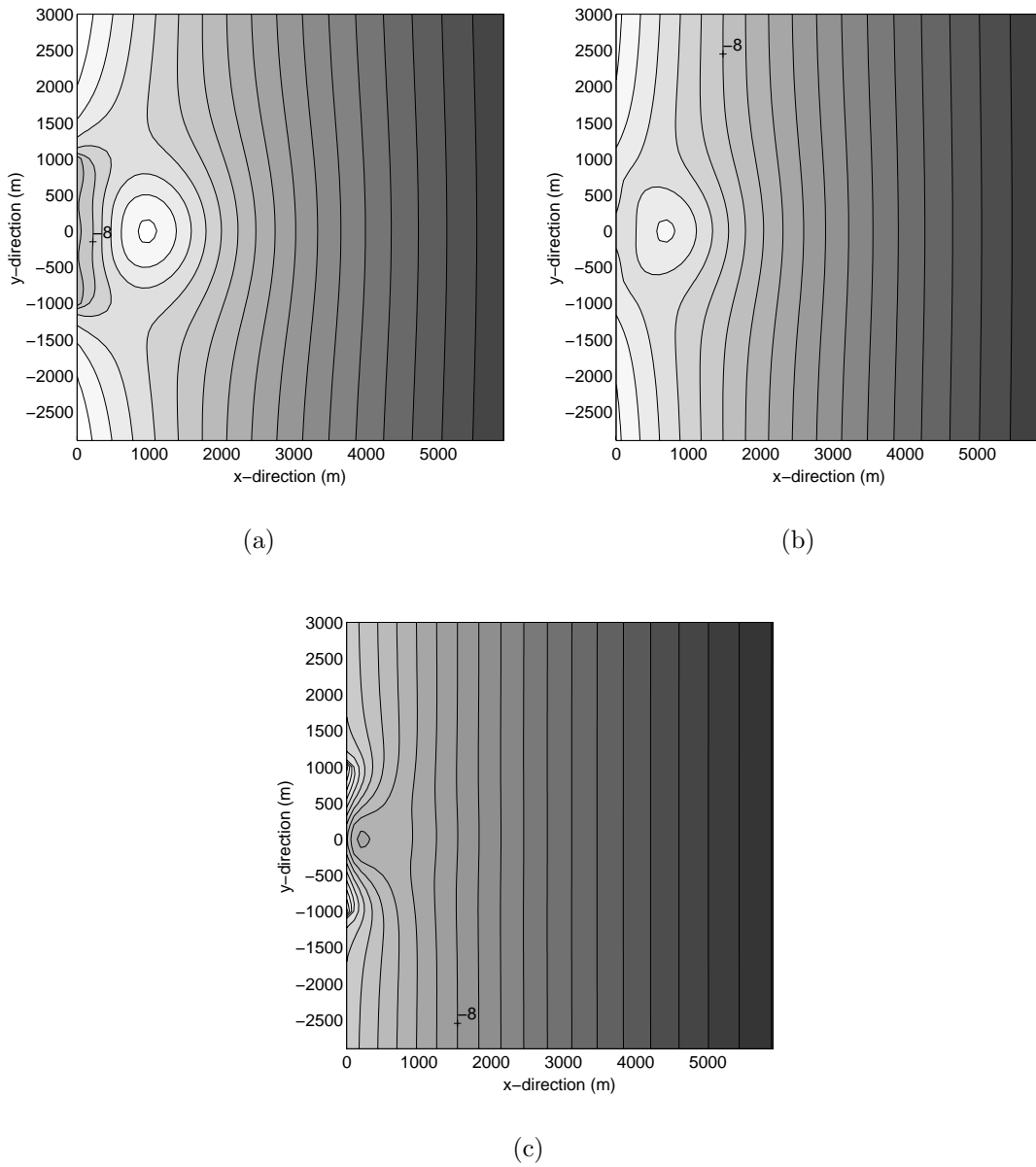
(a)



(b)



(c)

Figure 5.10: (a) Equilibrium bathymetry for experiment with zero phase difference between $M_2$ and $M_4$ tidal currents, $\phi = 0°$ (ebb-dominated case). Furthermore, in this experiment $U_{M_2} = 0.15$ ms$^{-1}$ and $U_{M_4} = 0.0375$ ms$^{-1}$ and velocity at the tidal inlet is prescribed according to Equation (5.29). For model setting and parameter values, see Tables 5.1-5.3. Contour lines are drawn every 0.5 m. (b) Same as (a), but now $\phi = 90°$ (no dominance). (c) Same as (a), but now $\phi = 180°$ (flood-dominated case).

offshore boundary. The values of the wave parameters are specified in Table 5.4. Other parameters are similar to the default parameter setting (Table 5.3), except for the value of $U_{M_2}$, $U_t$ and $U$. The typical velocity scales are: $U_t = U_{M_2}$, $U = \sqrt{U_t^2 + (u_{orb}/\beta)^2}$ and $U_{M_2} = 0.1$ ms$^{-1}$. The offshore wave parameters have been chosen such that $u_{orb}$ is near the inlet comparable to $U_{M_2}$. At the seaside boundary the waves have a significant wave

(a)                                                                        (b)
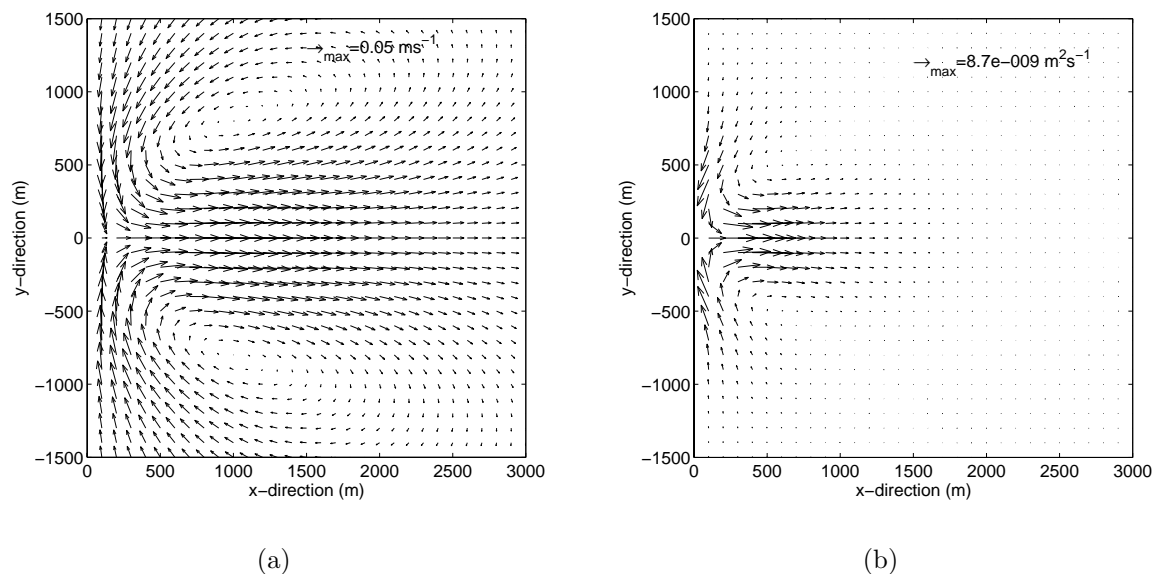
Figure 5.11:   Residual currents (a) and mean sediment transport $\vec{q}_f$ (b) for quadratic bottom stress at the first iteration step. $U_{M_2} = 0.2 \text{ ms}^{-1}$. For model setting and parameter values, see Tables 5.1-5.3.



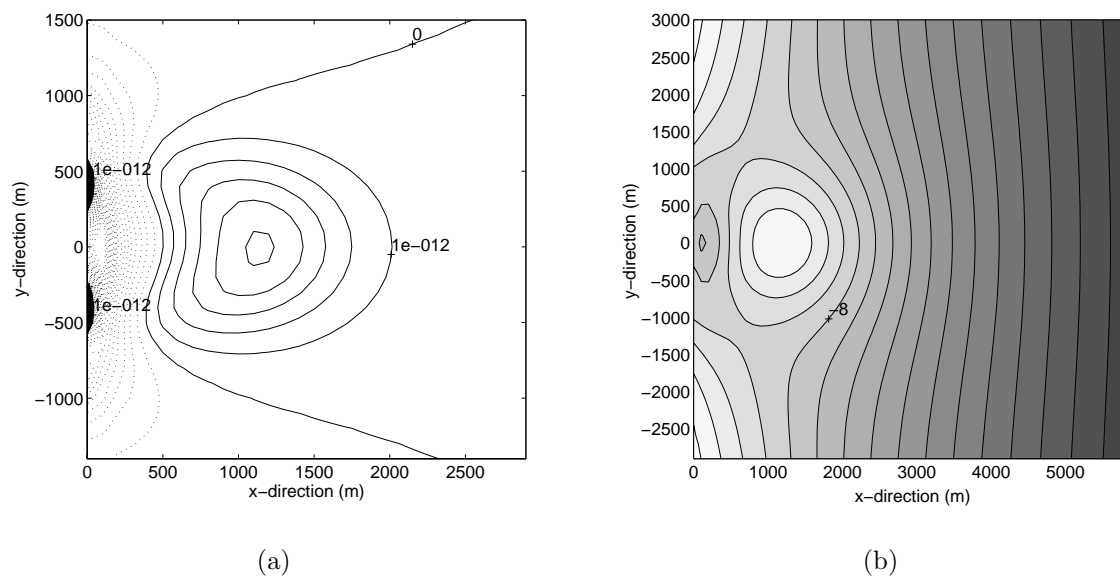(a)                                                                        (b)

Figure 5.12:   Experiment with quadratic bottom stress formulation, $U_{M_2} = 0.2 \text{ ms}^{-1}$. For model setting and parameter values, see Tables 5.1-5.3.(a) Convergence of the sediment transport in equilibrium, $-\vec{\nabla} \cdot \vec{q}_f$. Contour lines are drawn every $10^{-12} \text{ ms}^{-1}$. (b) Equilibrium bathymetry. Contour lines are drawn every 0.5 meter.

height of 0.21 m and a period of 7 s. The waves have shore-normal incidence and the directional spreading is 2 °. The influence of the currents on the waves is not included in the calculations. The wave parameters are used to calculate the bottom shear-stress
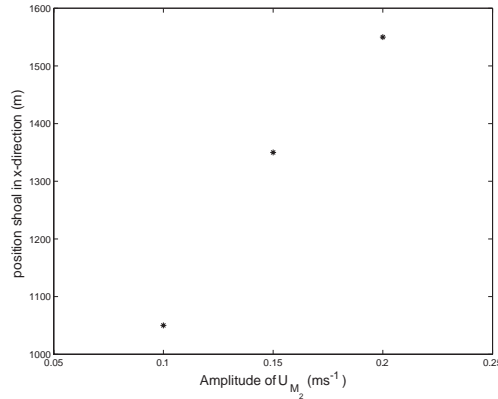
Figure 5.13:    The cross-shore position of the shoal against the amplitude of the prescribed cross-shore current in the experiment with quadratic bottom shear-stress.

experienced by the currents as described in Section 5.2.2. The sediment transport includes the effect of waves and is calculated using Equations (5.23a)-(5.23c).

| Variable | Choice |
|----------|--------|
| $H_{sig}$ | 0.21 m |
| $T_p$ | 7 s |
| dir | 90° |
| directional spreading | 2° |
| $U$ | $\sqrt{U_{M_2}^2 + |u_{orb}/\beta|^2}$ |
| $U_{M_2}$ | 0.1 ms$^{-1}$ |

Table 5.4:   Parameters for experiment with waves.

The wave parameters at the first iteration step are plotted in Figure 5.14. In this stage the bathymetry is $H = H_R(x)$. The top panel shows the bathymetry along the line $y = 0$. In the middle panels the significant wave height and the wave number $k$ are plotted. The wave height increases and the wave length decreases (so $k$ increases) when the water depth decreases. The lowest figure shows $u_{orb}$. It increases in shallower water. The radiation stresses, the dissipation of energy due to breaking and due to whitecapping is found to be very small.

The sediment transport pattern of $\vec{q}_{\text{res}}$ and $\vec{q}_a$ and the corresponding sediment erosion-deposition pattern are similar to those found in the previous experiments where waves were absent. There are differences, but these are small. A vector plot of the sediment transport $\vec{q}_{\text{wave}}$ is shown in Figure 5.15(a). The transport is clearly organized in two cells. Also far from the inlet ($\sim 1500$ m) the sediment transport rate is large. The convergence of $\vec{q}_{\text{wave}}$ is shown in Figure 5.15(b). In the center of the inlet sand is eroded. This area of erosion stretches diagonally out to the sides of the inlet. There are three distinct areas where sediment is deposited. One of them is located at 500-1500 m seaward of the tidal
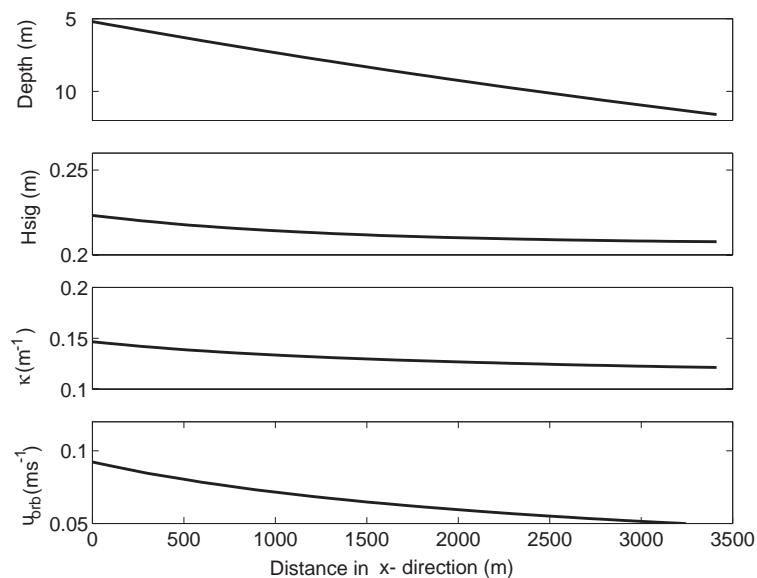
Figure 5.14:   Wave parameters for the initial iteration step ($H = H_{\mathrm{R}}$). The top panel shows the bathymetry along the line $y = 0$. The second panel shows the significant wave height. The third shows the magnitude of the mean wave number $|\vec{k}|$ and in the lowest panel $u_{orb}$ is plotted.

inlet, as was always found in the previous experiment. In addition, there are two areas with wave-induced sediment deposition at both sides of the inlet.
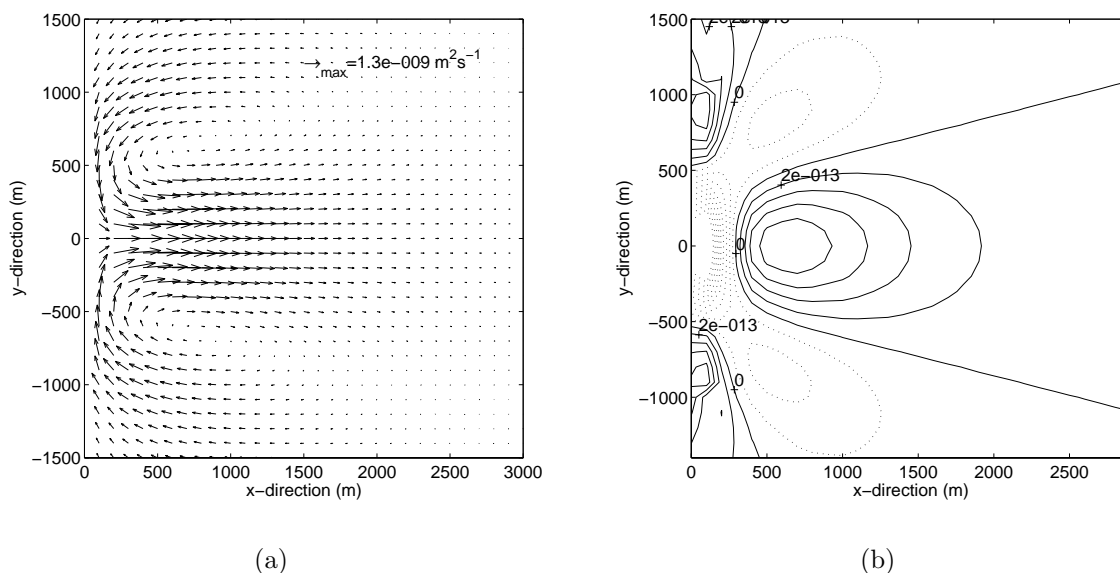


(a)                                                                                              (b)

Figure 5.15:   (a) Sediment transport due to waves ($\vec{q}_{\mathrm{wave}}$) in first iteration step. (b) Convergence $\vec{q}_{\mathrm{wave}}$. Contour lines are drawn every $2 \cdot 10^{-13}$ ms$^{-1}$.

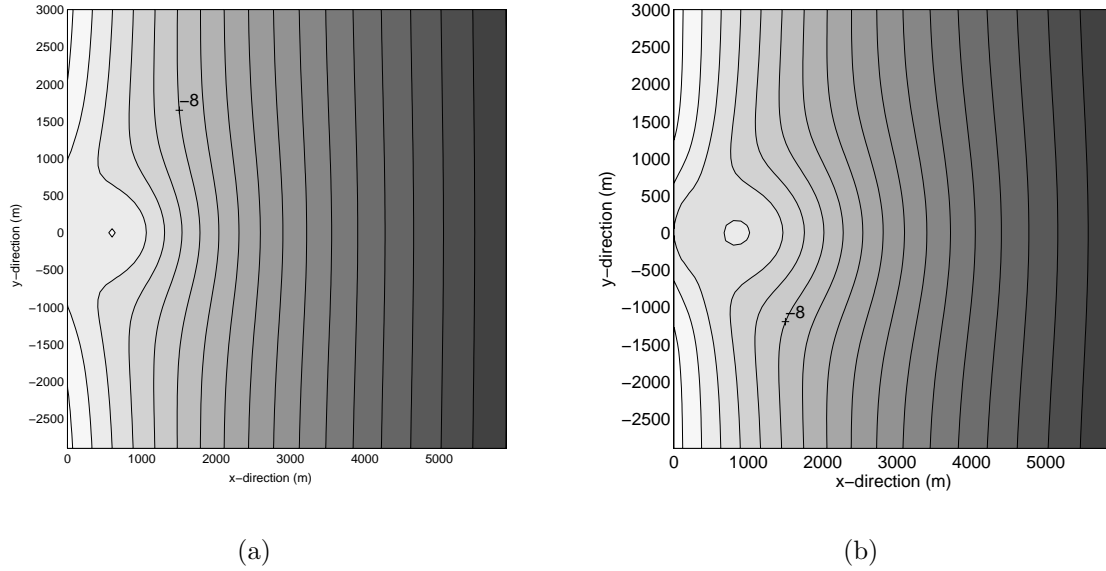(a)                                                             (b)

Figure 5.16:  (a) Equilibrium bathymetry for quadratic bottom stress and $U_{M_2} = 0.1$ ms$^{-1}$; no waves. (b) same as (a), but now with waves and parameters as defined in Table 5.4.

After 11 iterations morphodynamic equilibrium is reached. The equilibrium bathymetry is compared with that which is closest in parameter setting: $U_{M_2} = 0.1$ ms$^{-1}$, quadratic shear-stress and $\vec{q}_f$ calculated without the contribution of $\vec{q}_{\mathrm{wave}}$. The two equilibrium bathymetries are shown in Figure 5.16. The modeled shoal of the experiment with waves protrudes further into the sea (Figure 5.16(b)) compared to the experiment without waves (Figure 5.16(a)). Furthermore, the two flood-dominated channels are more pronounced.

At the first iteration step the wave parameters did not have alongshore variations and only were a function of the cross-shore coordinate. In equilibrium the wave parameters are influenced by the presence of the channels and the shoals. In Figure 5.17(a) a contour plot of the significant wave height $H_{sig}$ is shown. Above the shoal its value has increased more than 10 percent compared to its value at the first iteration. Note that $H_{sig}$ has decreased on the sides of the inlet compared to its values at the first iteration. In Figure 5.17(b) a contour plot of the magnitude of the wave orbital motion is shown. It has increased above the shoal and decreased again in the ebb-channel. A vector plot of $\vec{u}_w$ (defined in Equation (5.8)) is shown in Figure 5.17(c). The contour lines represent the equilibrium bathymetry. The alongshore components of $\vec{u}_w$ have been magnified by a factor 16. This is done to show that the waves refract towards the shallower delta. At the first iteration step the waves had a shore-normal direction. In equilibrium the waves can have an angle of 5° with respect to the normal of the coast.

Because the refraction of the waves is quite small and waves do not break (the ratio of wave height and water depth is very small), it is found that the divergence in the radiation stress tensor is small and no wave-driven currents are generated in this experiment.
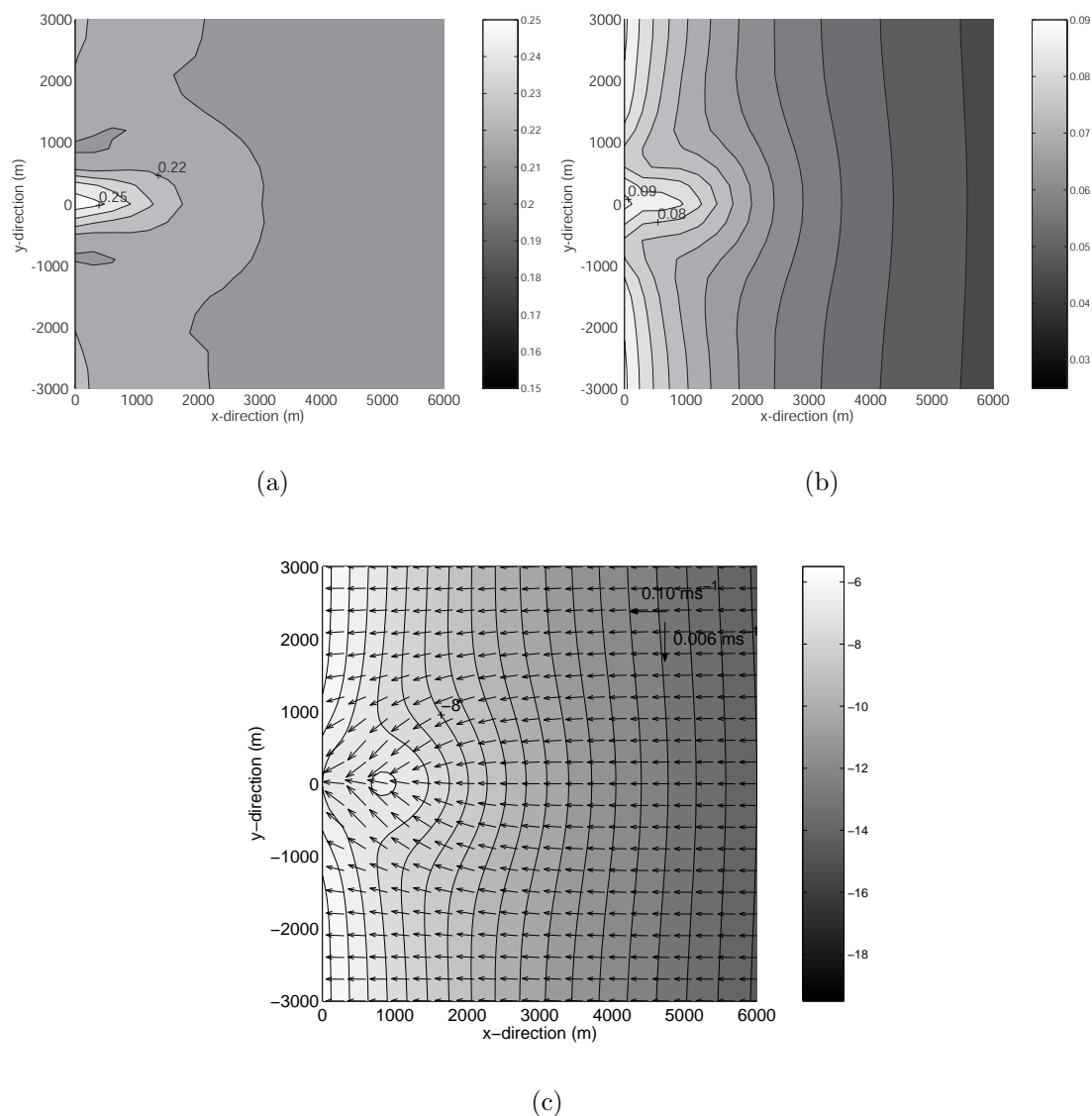
(a)



(b)



(c)

Figure 5.17: Wave parameters in equilibrium. (a) $H_{sig}$ (m). Light parts (dark parts) indicate large (small) significant wave height. Contour lines are drawn every 0.01 m. (b) Magnitude of the near-bed wave-orbital motion $u_{orb}$ (ms$^{-1}$). Light parts (dark parts) indicate large vales (small values) of $u_{orb}$. Contour interval is 0.01 ms$^{-1}$. (c) Vector plot of $\vec{u}_w$ (defined in Equation (5.8)). Its alongshore component is amplified by a factor 16. Furthermore, grey values indicate the depth. Dark is deep, light is shallow. Contour lines of depth are drawn every 0.5 meter.

# 5.5 Comparison of model results with observations and idealized model

## 5.5.1 Comparison with field data

In this section the characteristics of the modeled equilibrium bathymetries and water motion are compared with field data. In all the experiments the tidal flow during ebb

and flood has the same pattern, i.e. a jet-like flow during ebb and radial inflow during flood. This is consistent with the picture presented by *Stommel and Farmer* (1952) and *Oertel* (1975). *Wells and Van Heyst* (2003) observed similar behavior of water motion in a laboratory set-up. Quantitative comparison of the results with field data is difficult, since observed amplitudes of the tidal currents are much higher ( 1 ms$^{-1}$) than those used in the model. No reliable model solutions could be obtained for amplitudes of the tidal current larger than 0.3 ms$^{-1}$. This will be discussed in Section 5.6.

Except for the experiment with externally prescribed flood-dominated currents in the inlet, all modeled equilibrium bathymetries have a delta that is flanked by two flood-dominated channels. In the center of the tidal inlet a ebb-dominated channel is present. These findings are consistent with field observations (*Hayes*, 1975). There are, however, differences between the model results and the observations. In particular, the ebb-channel does not protrude as far seaward as observed in nature and the shoal does not bend around it. Adding higher harmonics of the tide to the sediment transport calculations and extending the model with a realistic description of the waves does not change the general picture of the equilibrium bathymetry. However, adding the quadratic bottom stress formulation results in a more seaward extension of the ebb-dominated channel and a first indication of the folding of the delta around it (Figure 5.12). For larger magnitudes of $U_{M_2}$ no morphodynamic equilibria are found and it can not be studied whether this effect becomes more pronounced.

The most quantitative comparison with observations possible is the comparison between the observed and modeled relation between the amount of sand stored in the ebb-tidal delta and the tidal prism. The tidal prism (TP) is defined as the total amount of water that flows through the inlet during one tidal cycle,

$$\text{TP} = \int_0^T \int_{-B/2}^{B/2} |\hat{U}(y,t)| H(0,y) dy dt. \tag{5.30}$$

The ebb-tidal sand volume (ESV) is defined as the total volume of sand above the reference bathymetry $H_R$

$$\text{ESV} = -\int \int_A [H(x,y) - H_R(x)]\Theta(H_R(x) - H(x,y)) dx dy, \tag{5.31}$$

where $\Theta$ is the Heaviside function and $A$ the model area. This means that only those areas with depths smaller than $H_R$ will contribute to ESV. The values of ESV and TP are made dimensionless by dividing the volumes by a control volume of 1 m$^3$. In Figure 5.18 some of the inlets presented by *Walton and Adams* (1976) are plotted (stars). They found a relation between ESV and TP using the data of more than 40 inlets at the US coast. This relation is

$$\text{ESV} = c_1 \text{TP}^{c_2} \tag{5.32}$$

with $c_1$ in the order of $10^{-2}$ and $c_2 = 1.23$. This empirical fit is shown in Figure 5.18 by the solid line. The power-like behavior is best seen when the logarithm is plotted of both TP and ESV. The modeled ESV as function of the modeled TP for the default parameter setting is shown by the black dotted line. The relation between ESV and TP

has the same slope as the observed slope, which implies that the power is close to that as found by *Walton and Adams* (1976). However, the modeled magnitudes of ESV are about a factor 3.5 smaller than observed. The fit of the model results yields $c_1 = 3 \cdot 10^{-3}$ and $c_2 = 1.23$. The modeled relation between ESV and TP for the experiment with quadratic bottom stress (dashed line in Figure 5.18) is even closer to the observations and the magnitude of the modeled sand volume is only a factor 2 smaller than observed. In this case the fit of the model results yields $c_1 = 1.1 \cdot 10^{-3}$ and $c_2 = 1.32$. The modeled sand volume with waves is larger than in the experiment without waves. It is denoted by an asterisk in Figure 5.18. The ebb-tidal sand volume in the experiment with waves is $7.5 \cdot 10^6$ m$^3$ and the tidal prism is $1.7 \cdot 10^7$ m$^3$. That result appears to agree quite well with the field data.
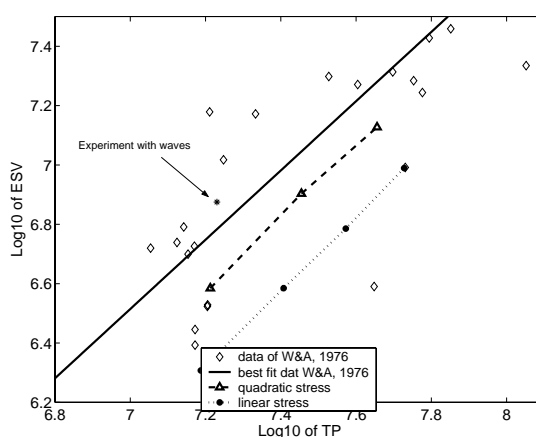


Figure 5.18: Ebb-tidal sand volume as a function of the tidal prism. Diamonds denote a part of the field data from *Walton and Adams* (1976). The solid line is the best fit of field data. The results of the quadratic stress experiments are denoted by the dashed line and those with the linear stress by the dotted line. The result of the experiment with waves is included as well.

## 5.5.2 Comparison with idealized model

The default experiment has been designed such that it is as close as possible to the idealized model as described in Chapter 3. In this section the results of the default case are compared with the results of the idealized model. In Figure 5.19(a) the flow patterns during ebb are shown. The black vectors show the currents calculated with the idealized model and the grey vectors denote the currents calculated with the numerical model. Both the numerical and idealized model generate an ebb-jet. The differences between the currents calculated with the numerical and with the idealized model are small. The largest differences are found in the region of the tidal inlet. The alongshore velocity components are smaller in the numerical model than in the idealized model. The ebb-jet is more pronounced in the numerical model than it is in the idealized model. During flood (Figure 5.19(b)) the modeled current patterns of the two models are almost similar. The differences are very small. The calculated residual currents are shown in Figure 5.19(c). Both models calculate two residual circulation cells of which the centers are located at

$(x, y) = (600, \pm 600)$. However, there are differences as well. The differences are largest in the region of the tidal inlet. The magnitudes of the residual currents are larger in the numerical model than in the idealized model. Close to the inlet the residual currents also have different direction.
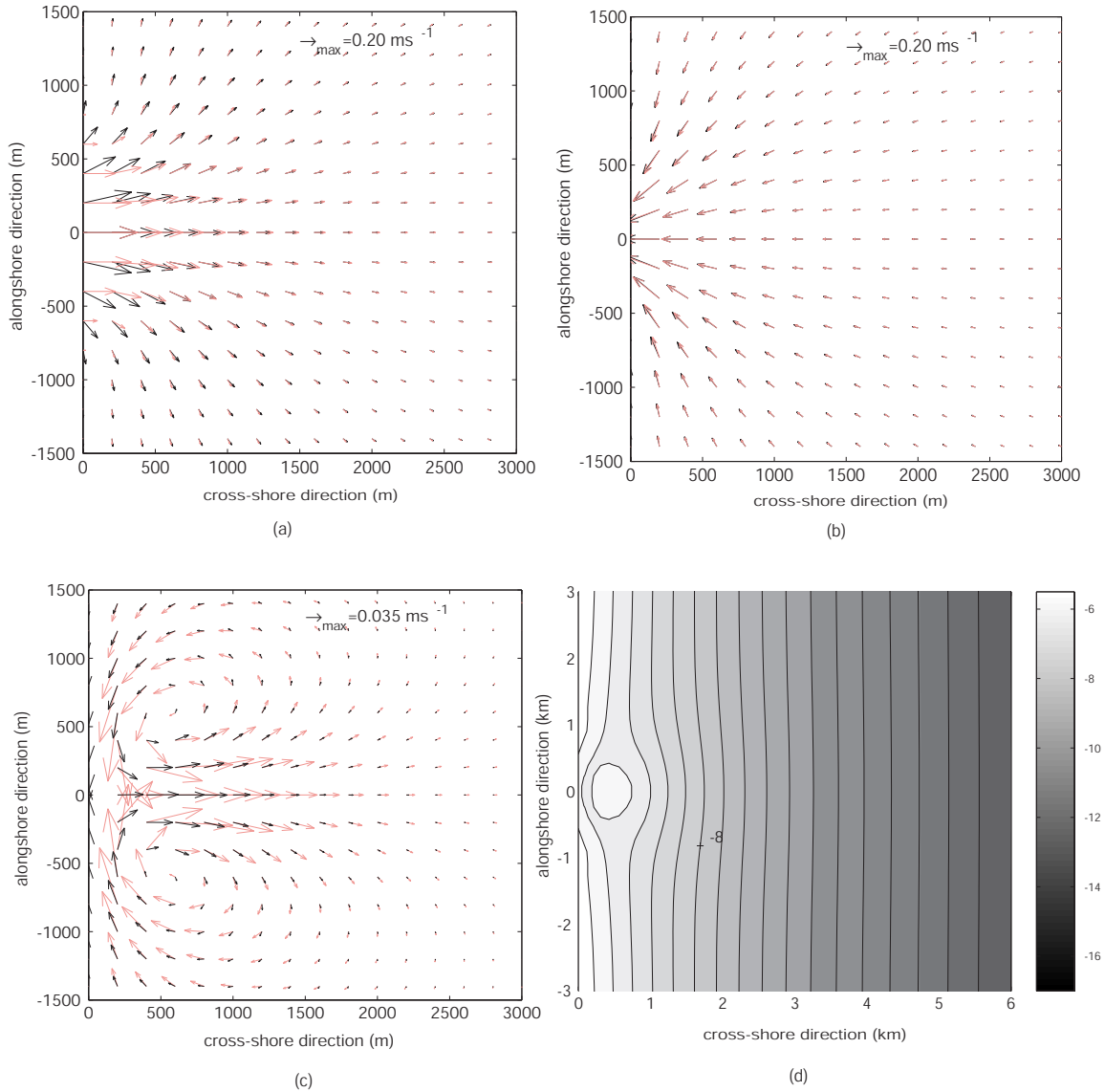


Figure 5.19:   Comparison of flow patterns in morphodynamic equilibrium obtained with idealized (black vectors) and with numerical model (grey vectors). (a) Maximum ebb. (b) Maximum flood. (c) Residual currents. (d) Equilibrium bathymetry for maximum tidal currents through the inlet of 0.2 ms$^{-1}$ and $B$=2km obtained with the idealized model.

Qualitatively, the differences between the modeled currents of the numerical and the idealized model are small. There are quantitative differences, however. Therefore, it can be expected that the modeled equilibrium bathymetries will differ quantitatively. The equilibrium bathymetry obtained with the idealized model is shown in Figure 5.19(d) and the one obtained with the numerical model in Figure 5.6(b). The results are very similar.

Both models reproduce the ebb-tidal delta at the end of the ebb-dominated channel. This delta is flanked by two flood-dominated channels. Quantitatively, there are differences. The minimum depth above the shoal in the idealized model is $\sim$ 6m at a cross-shore distance of 500 m. In the numerical model it is also $\sim$ 6 m, but the shoal is located 1000 m from the center of the tidal inlets. The bottom patterns are more pronounced, compared to the results of the idealized model.

### Model formulation

| Idealized model | Numerical model |
|---|---|
| Rigid lid approximation | $\zeta$ can be dynamically important |
| BC: In inlet $\partial v/\partial x = 0$ | Inflow: no tangential advection of momentum |
| | outflow: no extra BC |
| Infinite domain | Finite domain |

### Numerical method

| Idealized model | Numerical model |
|---|---|
| Space: Pseudospectral method | Finite differences |
| Time: Expansion in Fourier components | Standard time integrations |
| Truncation after $M_2$ harmonic component | "All" harmonic components included |

Table 5.5:   Main differences between "idealized" model and "realistic" model

To understand why these differences in model results occur it should be realized that, although both models were as close as possible in model formulation and parameter setting, there are still differences. These are summarized in Table 5.5. They concern the model formulation and the numerical methods to solve the equations. The first difference between both models is the use of a rigid lid approximation in the idealized model. This implies that in the idealized model only the pressure gradients due to the sea surface elevation are dynamically important. This is justified as long as the square of the Froude number ($Fr^2 = U^2/gH = \zeta/H$) is small. In Delft3D-FLOW this rigid lid approximation is not made. The results show that in the experiments the maximum sea surface elevation never exceeds 10 cm. Since the water depth is always more than 5 meter, this implies that $Fr^2 \sim 10^{-2}$. Therefore, the use of a rigid lid approximation in the idealized model is justified and it does not explain the differences between both models.

The second difference concerns the boundary conditions in the tidal inlet. In both models the cross-shore currents are prescribed, but the second condition is different: In the idealized model a free-slip condition is applied while in the numerical model during ebb the advection in the tangential direction is neglected and during flood no additional boundary condition is required. Neglecting the tangential advection is equivalent to assuming that the alongshore velocity is zero. This boundary condition forces a jet-like outflow during ebb. This is clearly visible in Figure 5.19(a). The numerical model has no alongshore component in the tidal inlet during ebb. During flood the numerical model computes a strong alongshore velocity component near the inlet. The residual currents calculated with the numerical model are larger than those obtained with the idealized model. Furthermore, the residual sediment transport and its convergence calculated with the numerical model are larger than those obtained with the idealized model. The con-

sequence is that the equilibrium bathymetry obtained with the numerical model is more pronounced than the one obtained with the idealized model.

The third difference is that the idealized model uses an infinite domain, while the numerical model uses a finite domain. This hardly influences the results, because the domain that is used in the numerical model is large enough to have vanishing currents and sediment transport at the seaward boundaries.

The fourth to sixth item listed in Table 5.5 concern the numerical method used to solve the models. In the idealized model a pseudospectral method is used, see Chapter 3. In the numerical model finite differences have been used. In the numerical model the free-slip condition at $x = 0$ is not well resolved. In the default experiment $A_h = 2.8$ m$^2$s$^{-1}$, resulting in a typical thickness of the boundary layer of $\sqrt{A_h/\sigma} \approx 140$ m. The grid size is 100 m. This might be too coarse to resolve the boundary layer. The idealized model does not suffer from this problem, because with the pseudospectral method the grid can be refined near $x = 0$. However, because the differences between flow pattern during flood calculated with the idealized model and calculated with the numerical model hardly differ, it is believed that this difference is not important.

The last difference between both models is introduced by the numerical method to solve the time-dependent part of the variables (fifth and sixth difference). In the idealized model a Galerkin method is used. The variables are expanded into a Fourier series. This series is truncated after the $M_2$ component. In the numerical model standard techniques are used and all components of the tide are calculated. The results obtained with the numerical mode show that there is only a very small generation of higher harmonics of the tide. Its relative magnitude is about 5% of the magnitude of the $M_2$ components. Therefore, the harmonic truncation is not likely to be responsible for large differences between the results obtained with both models.

The most important difference between the models seems to be the formulation of the boundary conditions in the inlet. This has been tested by performing an experiment in which the idealized model was forced by new boundary conditions at $x = 0$. The velocity field at $x = 0$ was prescribed with velocity components as calculated with the numerical model, retaining only the residual and $M_2$ components.

The current pattern during maximum ebb, maximum flood and the residual currents calculated with the adapted idealized model and the numerical model are shown in Figure 5.20. Black vectors are calculated with the adapted idealized model and grey vectors with the numerical model. The differences between the results obtained with the two model are much smaller than in the previous experiment. Especially during ebb the results have come much closer, while during flood the changed boundary conditions in the adapted idealized model hardly influences the calculated flow pattern. Furthermore, the residual currents calculated with the adapted idealized model and with the numerical model are in good agreement (Figure 5.20(c)). However, especially near the tidal inlet the vectors still do not have the same magnitude and direction. The equilibrium bathymetry calculated with the adapted idealized model is shown in Figure 5.20(d). The channels calculated with the numerical model are still a little deeper and the position of the shoal is further seaward, but the differences between the idealized and the numerical are much smaller than in the previous experiment (see Figure 5.19(d)).
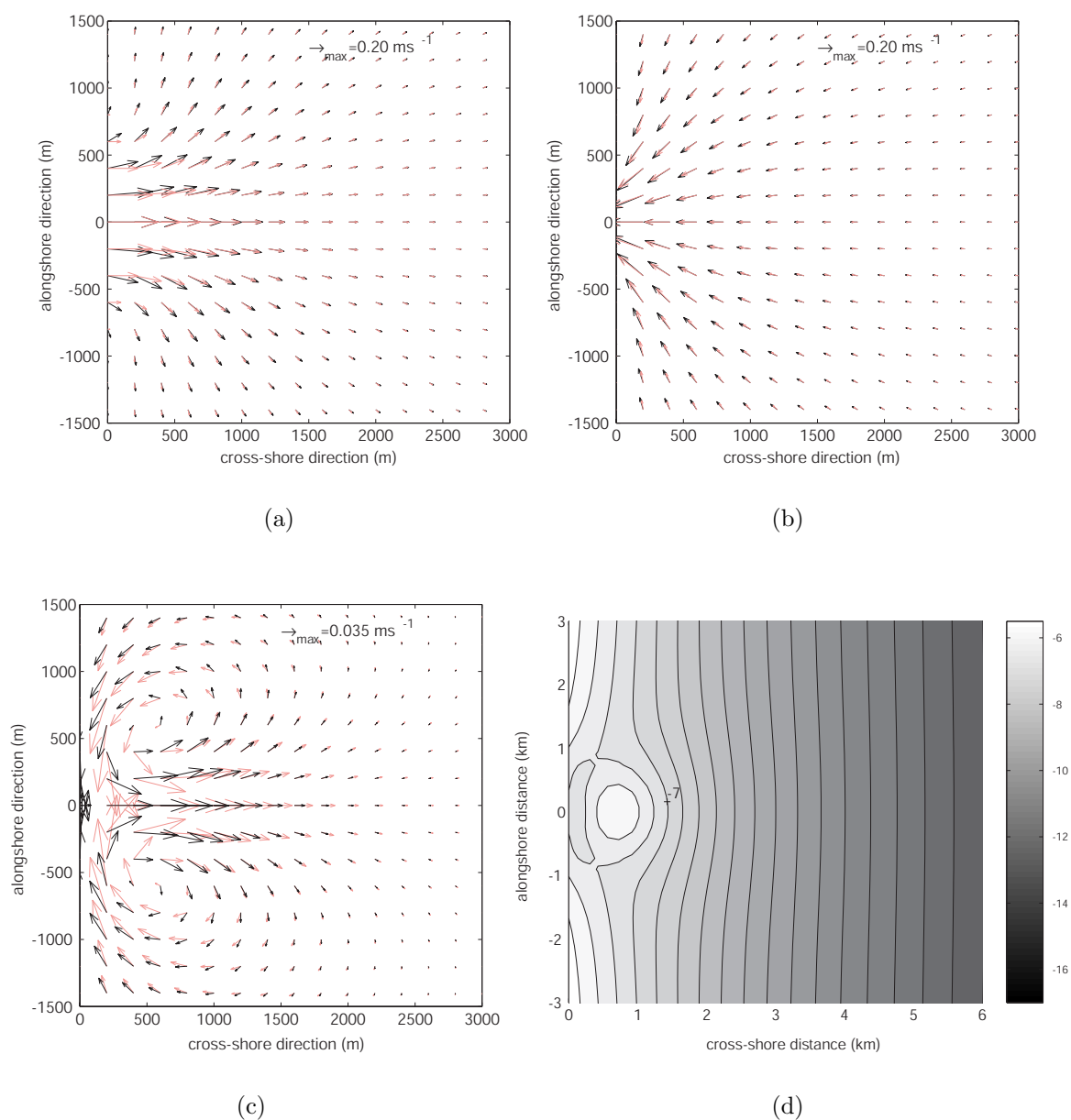
Figure 5.20: Comparison of model results in morphodynamic equilibrium obtained with the adapted idealized model and with numerical model. The velocity field obtained with the numerical model in the default case has been used as a boundary condition at the coastline for the adapted idealized model. (a) Currents during maximum ebb (black vectors represent idealized model, grey vector numerical model). (b) As (a), but now during maximum flood. (c) As (a). but now the residual currents. (d) Equilibrium bathymetry calculated with the adapted idealized model. Contour lines every 0.5 m.

## 5.6   Discussion

The objectives for the study described in this chapter were twofold. The first was to develop a numerical morphodynamic model which allows for equilibrium solutions. The

results of this model were compared with observations and with the results obtained with the idealized model described by *van der Vegt et al.* (2005). The second was to study the sensitivity to processes that could not be accounted for in the idealized model. A detailed comparison of model results with observations and with the idealized model was presented in the previous section. Here, the sensitivity of the results to extensions in the model formulation are discussed. After this, it is discussed why for $U_{M_2} > 0.3$ ms$^{-1}$ no morphodynamic equilibria were found.

### Sensitivity to tidal asymmetry

The influence of internally generated higher harmonics on the morphodynamic equilibrium turns out to be small. The additional sediment transport due to higher harmonics of the tide, $\vec{q}_a$, is in the order of 10 %. In *van de Kreeke and Robaczewska* (1993) it was shown that in the one-dimensional case the magnitude and direction of $\vec{q}_a$ depends on the magnitude of the $M_4$ and $M_2$ tidal currents and on their relative phase difference. In the two-dimensional case the expressions for $\vec{q}_a$ become more elaborate (*van der Molen*, 2000). But also in that analysis $\vec{q}_a$ is a function of the magnitude of the $M_4$ and $M_2$ tidal currents. The magnitude of the $M_4$ currents is measured by the long axis of the $M_4$ tidal current ellipse. Its maximum in the domain is 0.013 ms$^{-1}$, which is about a factor 3 smaller than the maximum residual currents (0.035 ms$^{-1}$). Moreover, there is an approximate phase difference of 90° between the $M_2$ and $M_4$ tidal currents. This results in only a small contribution of $\vec{q}_a$ to $\vec{q}_f$.

The influence of an externally prescribed $M_4$-component on the calculated morphodynamic equilibria is much stronger. Depending on the phase difference $\phi$ between the $M_2$ and $M_4$ tidal current, the equilibrium bathymetry has no shoal or a larger shoal compared to the situation without externally forced $M_4$ current. When $\phi = 0°$ the ebb-dominated channel is deeper and the shoal is larger and is located further seaward. This is caused by the additional sediment transport due to the higher harmonics of the tide. In the case that $\phi = 90°$, the tidal currents during ebb have the same magnitude as during flood and the net sediment transport $\vec{q}_a$ is very small. For $\phi = 180°$ the currents in the inlet are flood-dominated. The convergence of $\vec{q}_a$ causes erosion in the whole domain. This erosion is larger than the deposition of sediment induced by the convergence of $\vec{q}_{\mathrm{res}}$. This results in the absence of an ebb-tidal delta. This prediction seems to be in correspondence with observations. It is found that that inlets with strong flood-dominated currents only have poorly developed ebb-tidal deltas, whereas deltas with ebb-dominated currents have large ebb-tidal deltas (*Walton*, 2002).

### Sensitivity to quadratic bottom shear-stress

The results obtained with the numerical model are sensitive to the use of the quadratic bed shear-stress formulation instead of the linearized one. The magnitude of the residual currents obtained with the quadratic bottom stress formulation are larger than in the default case. Furthermore, the spatial extensions of the two residual circulation cells are increased compared to the default experiment. The linearized bottom stress formulation is normally motivated by an energy consideration: The dissipation of kinetic energy per

tidal period obtained with the linearized bottom stress formulations should equal the dissipation as obtained with a quadratic formulation. Therefore, the tidally averaged dissipation of kinetic energy is calculated for both the linearized and the quadratic bottom shear-stress formulation. This is done for the first iteration step in the case that $U_{M_2} = 0.2$ ms$^{-1}$. The tidally averaged energy dissipation $D_{\mathrm{lin}}$ obtained with the linearized stress is

$$D_{\mathrm{lin}}(x,y) = \frac{8}{3\pi} \frac{gU}{C_z^2 T} \int_{t=0}^{t=T} |\vec{u}(x,y,t)|^2 dt \qquad (5.33)$$

The energy dissipation $D_{\mathrm{qua}}$ obtained with the quadratic bottom shear-stress is

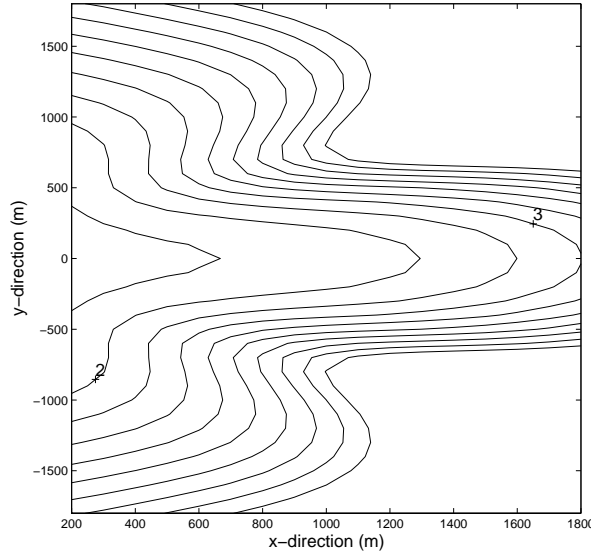$$D_{\mathrm{qua}}(x,y) = \frac{g}{C_z^2 T} \int_{t=0}^{t=T} |\vec{u}(x,y,t)|^3 dt \qquad (5.34)$$



Figure 5.21: Comparison between the tidally averaged dissipation of energy obtained with linear and with quadratic bottom shear-stress, $D_{\mathrm{lin}}/D_{\mathrm{qua}}$. Contour lines indicate the factor of overestimation in the linear bottom stress. Contour lines every 0.5.

In Figure 5.6 a contour plot of the ratio of $D_{\mathrm{lin}}$ and $D_{\mathrm{qua}}$ is shown. Only in the middle of the inlet the energy dissipation due to the linearized bottom shear-stress equals that of the quadratic stress. In the rest of the domain the dissipation due to the linearized stress is substantially larger. This has importance consequences for the residual velocity. In *Zimmerman* (1981) it is shown that residual circulation cells are strongly related to tidally averaged vorticity. In *van der Vegt et al.* (2005) it was shown that the main balance in the tidally avaraged vorticity balance is between the convergence in the vorticity flux (which generates residual vorticity) and the dissipation of residual vorticity by friction. When the energy dissipation by friction is overestimated, the residual vorticity will be underestimated. This results in smaller residual currents, smaller sediment transport and a smaller convergence of it. As a consequence, the modeled equilibrium bathymetry is

smaller. In conclusion, the estimate of $U$ in Equation (5.14) leads to a strong overestimation of the energy dissipation due to linearized bottom friction and an underestimation of the magnitude of the residual currents. A better estimate is needed. Since the magnitudes of the tidal currents strongly vary in the region of the tidal inlet, it is recommended to apply the Lorentz linearization procedure at each position in the domain. This will result in a spatially dependent $U$. This is in principle possible with the idealized model.

**Sensitivity to waves**

The last extension of the model is the incorporation of a realistic description of the waves. This leads to flood channels which are more pronounced (deeper) and to a shoal which lies further seaward compared to the experiment without waves. The depth above the shoal is still relatively deep and the waves are small. Therefore the waves do not break and no wave-driven currents are generated. However, the refracting of the waves towards the shoal is visible (Figure 5.17(c)). In the case that the depth above the shoal decreases or the wave height increases it is expected that these kind of effects will become more important. The waves will refract to and ultimately break above the shoal. This will result in wave-driven currents that will affect the modeled equilibrium bathymetry. For realistic scenarios the numerical model yields more accurate results than the idealized model.

**Why no convergent solutions for $U_{M_2} > 0.3$ ms$^{-1}$?**

In this study convergent solutions are found for $U_{M_2}$ up to a maximum of 0.30 ms$^{-1}$. Interestingly, with the idealized model morphodynamic equilibria were found for much higher velocity amplitudes. This raises the question why the numerical model does not allow for equilibrium solutions for $U_{M_2} > 0.3$ ms$^{-1}$.

There are two possible explanations. The first is related to the numerical methods to solve the model. As was already discussed in Section 5.5.2, the grid size of 100 meter might be too coarse to calculate the patterns in the convergence of the sediment transport in the region of the tidal inlet. Furthermore, the free-slip condition at $x = 0$ is not well resolved. The input of tidal vorticity is a very important parameter for the generation of residual circulation cells (*van der Vegt et al.*, 2005). In turn, the residual currents are important for the residual sediment transport and its convergence. In the idealized model the boundary conditions in the inlet are such that the input of vorticity into the domain is determined by the shear in the velocity profile prescribed in the inlet. In the numerical model this is not the case because $\partial v/\partial x$ is to be determined by the model. If the coupling between the bottom and vorticity input is very nonlinear, a small change in the magnitude of the bottom patterns can result in a large change of the vorticity input and a large change of the current patterns. The iterative solution procedure fails to calculate the morphodynamic equilibria. However, with the idealized model also above a certain magnitude of the cross-shore tidal currents no equilibria were found. Therefore, another explanation should be considered as well.

The second explanation concerns the possible existence of bifurcations in parameter space. These bifurcations have been found in previous studies for tidal basins (*Schuttelaars*

*and de Swart*, 2000; *Schramkowski et al.*, 2004). Although in these studies other problems have been studied, the system studied in this chapter has strong similarities in model formulation. When bifurcations exist, it might be that equilibria exist for $U_{M_2} > 0.3 \text{ ms}^{-1}$, but the differences with the equilibrium of a slightly smaller parameter are so large, that the continuation method fails to find the equilibrium for this parameter setting. A stability analysis has to be performed to obtain insight in the existence of these bifurcations or more sophisticated continuation techniques should be used.

## 5.7 Conclusions

In the previous section the main results already have been discussed. In this section a short summary of the main findings is given. The section ends with suggestions for further research.

The first objective of this study was to validate the results of the idealized model by calculating morphodynamic equilibria with a numerical model. The results presented in Section 5.4.2 and the discussion of Section 5.5.2 show that both models yield similar results. The main (quantitative) differences are caused by the boundary conditions at the tidal inlet which could not be made equivalent. It is concluded that the the rigid-lid approximation, as used in the idealized model, is valid.

The second objective of this study was to investigate the sensitivity of the results to higher harmonics of the tide, quadratic bottom shear-stress and to waves of which the properties are obtained with a realistic wave model. The results presented in Section 5.4.4 showed that the influence of internally generated higher harmonics is small. However, externally prescribed higher harmonics can have a large influence on the calculated mor-phodynamic equilibria. In the case that the currents in the inlet were ebb-dominated the bottom patterns were more pronounced. In the case of flood-dominated currents the ebb-tidal delta can be absent. In Section 5.4.5 it was shown that using a quadratic bot-tom shear-stress formulation instead of a linearized one results in a larger ebb-tidal delta. Furthermore, the cross-shore length of the ebb-dominated channel was larger and a first indication was seen that the ebb-tidal delta folds around the ebb-dominated channel. In addition, the modeled ESV was closer to observed values than when a linearized bottom shear-stress formulation is used. The analysis presented in Section 5.6 showed that the linearized bottom shear stress formulation as used in the idealized model overestimates the dissipation of momentum due to friction. It was concluded that the linearized stress formulation can only be used if at each position in the domain a linearization procedure is applied, which will result a spatially dependent magnitude of $U_t$. The results presented in Section 5.2.2 showed that already for small waves processes like refraction become notice-able. From these results it is expected that for realistic scenarios a state-of-the-art wave model should be used, instead of the highly idealized version that is used in the idealized model.

Although the numerical model uses a realistic description for the waves and currents, other aspects of the model are still idealized. In the inlet the velocity was prescribed. This velocity did not change when the bathymetry changed. Hence, the interaction between the inner basin and the ebb-tidal delta is not modeled. A more realistic set-up can be

achieved when a strait connects the sea with a tidal basin. In that case the sea and basin can dynamically interact and the velocity in the strait would follow from physical laws.

Another important simplification of the model is the use of a spatially independent $U$ and $U_t$. Therefore, $\vec{q}_{\text{bot}}$ only has spatial variations due to spatial variations in $H'$. The analysis of the results obtained with the quadratic bottom shear-stress formulation show that a constant $U_t$ is not a very good approximation. It would be better to use a spatially dependent $U_t$. If also a spatially dependent $U$ is used, this will strongly affect the calculation of $\vec{q}_{\text{bot}}$ and the calculation of the equilibria, as was already shown in Chapter 3. Moreover, in this study only one (bedload) sediment transport formulation has been studied. There are many other formulations for the sediment transport, which also include suspended-load sediment transport formulations. These need to be considered as well.

The last aspect that has to be mentioned here is that the processes that lead to asymmetry have been excluded. A thorough study of these processes is needed because many observed deltas are asymmetric. The morphodynamic model discussed in this chapter leaves many possibilities to systematically study the mechanisms that lead to asymmetry of ebb-tidal deltas. Moreover, the numerical model can in principle also be used to calculate morphodynamic equilibria for other areas such as tidal basins.